Titre: Title:	Multinozzle Architecture for Additive Manufacturing of High-Viscosity Thermosets for Aerospace Applications
Auteur: Author:	Raphaël Plante
Date:	2026
Type:	Mémoire ou thèse / Dissertation or Thesis
Référence: Citation:	Plante, R. (2026). Multinozzle Architecture for Additive Manufacturing of High-Viscosity Thermosets for Aerospace Applications [Mémoire de maîtrise, Polytechnique Montréal]. PolyPublie. https://publications.polymtl.ca/76260/

URL de PolyPublie: PolyPublie URL:	https://publications.polymtl.ca/76260/
Directeurs de recherche: Advisors:	Daniel Therriault, & Sampada Bodkhe
Programme: Program:	Génie mécanique

POLYTECHNIQUE MONTRÉAL

affiliée à l'Université de Montréal

Multinozzle Architecture for Additive Manufacturing of High-Viscosity Thermosets for Aerospace Applications

RAPHAËL PLANTE

Département de génie mécanique

Mémoire présenté en vue de l'obtention du diplôme de *Maîtrise ès sciences appliquées*

Génie mécanique

Avril 2026

POLYTECHNIQUE MONTRÉAL

affiliée à l'Université de Montréal

Ce mémoire intitulé :

Multinozzle Architecture for Additive Manufacturing of High-Viscosity Thermosets for Aerospace Applications

présenté par **Raphaël PLANTE**

en vue de l'obtention du diplôme de *Maîtrise ès sciences appliquées*

a été dûment accepté par le jury d'examen constitué de :

Farbod KHAMENEIFAR, président

Daniel THERRIAULT, membre et directeur de recherche

Sampada BODKHE, membre et codirectrice de recherche

Dmitri FEDOROV, membre

ACKNOWLEDGEMENTS

I would first like to express my sincere gratitude to my supervisor, Prof. Daniel Therriault, for his mentorship throughout this master's project. His enthusiasm, high standards, and constant support created an environment that was both demanding and motivating. I am especially grateful for the many opportunities he provided, including conference participation, and for the confidence he placed in my work.

I also wish to thank my co-supervisor, Prof. Sampada Bodkhe, for her guidance and thoughtful feedback. Her perspective often complemented that of my supervisor and helped me view my work from different angles.

My sincere thanks also go to Rouhollah D. Farahani for his availability, insight, and steady support throughout the project. I am particularly grateful for the time he devoted to reviewing my written work and for the encouragement he provided at important moments.

I would also like to thank my colleagues at the Laboratory for Multiscale Mechanics (LM^2). The atmosphere of the laboratory was one of the main reasons I chose this research group, and it remained one of its greatest strengths throughout my studies. I am especially grateful to Loïc, Mathieu, and Negar for their friendship, their advice, and the many helpful discussions we shared. I would also like to thank Ruby Rozier and Vikram Roussel for their help during experiments. Having others to think through problems with, and to share the workload of long experimental sessions, made a real difference.

I am deeply grateful to my partner, Justine Trudel, for her constant support throughout this project. Her feedback was always valuable. More importantly, her love, discipline and focus were a constant source of motivation.

I also wish to thank my parents for their unconditional support throughout my studies. Their encouragement and patience made this work possible. Whether by listening to my ideas, my presentations, or simply supporting me throughout the process, they helped me more than they probably realize. Finally, I would like to thank my sisters for their support and encouragement throughout my studies, and especially Rosalie for the genuine interest she took in my project and for always being willing to listen when I needed to talk through an idea or prepare for an oral presentation.

RÉSUMÉ

Au cours des dernières années, la fabrication additive de polymères et de composites a suscité un intérêt croissant pour la production de structures légères, complexes et multifonctionnelles. Dans le domaine aérospatial, l'écriture directe d'encre « Direct Ink Writing, DIW » apparaît comme une voie prometteuse pour la fabrication de réseaux filamentaires architecturés à partir de matériaux thermodurcissables visqueux, notamment pour des revêtements abradables structurés. Toutefois, la mise en forme de telles structures demeure limitée par la faible cadence généralement associée à la DIW à fine résolution. Bien que des solutions aient été proposées pour accroître cette cadence, notamment par l'emploi de systèmes multibuses, la résistance hydraulique imposée par la géométrie interne des buses reste encore peu considérée. Or, lorsque la pression d'extrusion disponible est limitée, cette résistance devient un verrou important du procédé. Ce projet vise donc le développement, sur la plateforme robotisée de fabrication additive du Laboratoire de Mécanique Multi-échelle (LM2), d'une architecture multibuse conique compatible avec une limite pratique de pression de 20 MPa. L'objectif est de remplacer la multibuse cylindrique développée précédemment au laboratoire par une architecture mieux adaptée aux contraintes hydrauliques du système. La solution développée repose sur une architecture multibuse effilée fabriquée par stéréolithographie et comprenant une grille 6 × 6 de 36 buses coniques. Afin de rendre cette géométrie compatible avec les sollicitations mécaniques imposées par l'extrusion sous haute pression, le composant polymère définissant l'écoulement est soutenu par une plaque de support métallique réutilisable située hors du chemin d'écoulement. Cette dissociation entre fonction hydraulique et fonction structurale permet à la fois l'intégration d'un réseau dense de canaux convergents et le remplacement rapide du composant en contact avec l'encre. La caractérisation de la multibuse imprimée montre que la fabrication par SLA permet d'obtenir des sorties proches de la géométrie nominale, avec des diamètres moyens mesurés de 255,7 ± 14,1 µm pour la géométrie nominale de 230 µm et de 370,0 ± 22,5 µm pour celle de 350 µm. Les observations montrent également une bonne circularité des ouvertures ainsi qu'une faible rugosité interne des canaux, avec une valeur moyenne de Ra = 0,50 ± 0,21 µm. Ces résultats confirment qu'il est possible de fabriquer par SLA une tête multibuse à sorties fines présentant une fidélité dimensionnelle et une qualité de surface suffisantes pour l'extrusion. L'architecture proposée a ensuite été évaluée avec trois encres représentatives : une encre organique de référence, une formulation thermodurcissable EPON 828-14%FS et un composite thermodurcissable industriel EC3515-10%FS. Par rapport à la multibuse cylindrique de référence, la géométrie effilée a réduit la pression requise de 71,6 % pour l'encre organique et de 84,6 % pour la formulation EPON 828-14%FS à une vitesse d'extrusion de 200 mm/s. Pour l'EC3515-10%FS, la fabrication d'un micro-échafaudage périodique a été possible à 100 mm/s pour environ 11 MPa avec les buses nominales de 350 µm, alors que des configurations cylindriques comparables n'étaient pas opérables sous la limite de pression disponible. Dans ces conditions, la vitesse de dépose obtenue avec 36 buses correspond à un débit total supérieur à 500 mm^3/s, tout en permettant le dépôt de filaments de moins de 500 µm de diamètre. Une portion représentative de micro-échafaudage, constituée de 18 couches de 108 filaments parallèles espacés de 1 mm, a été fabriquée en moins de 3,5 minutes. Le micro-échafaudage obtenu présente un écart moyen de +20,0 µm des points de sa surface par rapport à la géométrie cible, et 85,6 % de ces se situent à l'intérieur d'une bande de ±100 µm. À plus grande échelle, l'analyse d'une structure planaire représentative indique qu'une configuration à 36 buses pourrait réduire le temps de fabrication estimé de 40,8 h avec une seule buse à 1,1 h à vitesse de dépose identique, ce qui souligne l'intérêt de la parallélisation. L'ensemble de ces résultats montre qu'une architecture multibuse conique imprimée par SLA constitue une approche crédible pour améliorer l'efficacité hydraulique de l'écriture directe d'encre, en réduisant fortement la pression requise et en augmentant le débit de dépose. Ce travail illustre ainsi comment une technologie de fabrication additive peut être mobilisée pour en améliorer une autre, tout en contribuant au développement de systèmes DIW multibuses plus accessibles, plus facilement remplaçables et moins exigeants sur le plan de la pressurisation.

ABSTRACT

Over the past several years, additive manufacturing of polymers and composites has attracted growing interest for the production of lightweight, complex, and multifunctional structures. In aerospace applications, Direct Ink Writing (DIW) has emerged as a promising approach for fabricating architectured filament networks from viscous thermosetting materials, particularly for structured abradable coatings. However, the fabrication of such structures remains limited by the low build rates generally associated with fine-resolution DIW. Although solutions such as multinozzle systems have been proposed to increase throughput, the hydraulic resistance imposed by nozzle internal geometry remains comparatively underexplored. When the available extrusion pressure is limited, this resistance becomes a major process constraint.

This project therefore focuses on the development, on the existing robotic additive manufacturing platform of the Laboratory of Multiscale Mechanics (LM2), of a tapered multinozzle architecture compatible with a practical pressure limit of 20 MPa. The objective is to replace the cylindrical multinozzle previously developed at the laboratory with a geometry better suited to the hydraulic constraints of the system. The proposed solution consists of a stereolithography-fabricated tapered multinozzle architecture comprising a 6 × 6 array of 36 outlets. To withstand the mechanical loads associated with high-pressure extrusion, the polymer component defining the flow is supported by a reusable metallic backing plate located outside the flow path. This separation of hydraulic and structural functions allows both the integration of a dense network of converging channels and rapid replacement of the ink-contacting component. Characterization of the printed printhead shows that SLA fabrication can produce outlets close to the nominal geometry, with measured mean diameters of 255.7 ± 14.1 μm for the nominal 230 μm design and 370.0 ± 22.5 μm for the nominal 350 μm design. The observations also revealed good outlet circularity and low internal channel roughness, with an average Ra of 0.50 ± 0.21 μm. These results confirm that SLA can be used to fabricate a fine-outlet multinozzle printhead with sufficient dimensional fidelity and surface quality for extrusion. The proposed architecture was then evaluated using three representative inks: a reference organic ink, an EPON 828-14%FS thermosetting ink, and an industrial EC3515-10%FS thermosetting composite ink. Relative to the cylindrical reference multinozzle, the tapered geometry reduced the required pressure by 71.6% for the organic ink and by 84.6% for the EPON 828-14%FS ink at an extrusion speed of 200 mm/s. For EC3515-10%FS, the fabrication of a periodic microscaffold was achieved at 100 mm/s at approximately 11 MPa using nominal 350 μm

outlets, whereas comparable cylindrical configurations were not operable within the available pressure limit. Under these conditions, deposition through 36 outlets corresponds to a total flow rate greater than 500 mm^3/s while still producing filaments below 500 µm in diameter. A representative microscaffold section consisting of 18 layers of 108 parallel filaments spaced 1 mm apart was fabricated in less than 3.5 minutes. The resulting microscaffold showed a mean surface deviation of +20.0 µm from the target geometry, and 85.6% of its surface points fell within a ±100 µm tolerance band. At a larger scale, analysis of a representative planar structure indicates that a 36-nozzle configuration could reduce the estimated fabrication time from 40.8 h with a single to 1.1 h at the same deposition speed, further highlighting the value of parallelization.

Taken together, these results show that an SLA-fabricated tapered multinozzle architecture is a credible route for improving the hydraulic efficiency of Direct Ink Writing by substantially reducing the required pressure while increasing deposition rate. More broadly, this work illustrates how one additive manufacturing technology can be used to improve another, while contributing to the development of multinozzle DIW systems that are more accessible, more easily replaceable, and less demanding in terms of pressurization.

TABLE OF CONTENTS

ACKNOWLEDGEMENTS iii

RÉSUMÉ iv

ABSTRACT vi

TABLE OF CONTENTS viii

LIST OF TABLES xi

LIST OF FIGURES xii

LIST OF SYMBOLS AND ABBREVIATIONS xvi

LIST OF APPENDICES xviii

CHAPTER 1 INTRODUCTION 1

1.1 Project Context 1

1.2 Research Objectives 4

1.3 Thesis Outline 4

CHAPTER 2 LITERATURE REVIEW 5

2.1 Additive Manufacturing and the Place of Direct Ink Writing 5

2.2 Rheology and Printability in DIW 6

2.3 Extrusion of Highly Viscous, Filled, and Thermosetting Inks 7

2.4 Nozzle Geometry and Hydraulic Resistance in DIW 9

2.5 Multinozzle Architecture in DIW 10

2.6 Manufacturing Routes for Multinozzle Printheads 13

2.7 Synthesis and Research Gap 17

CHAPTER 3 METHODOLOGY AND SCOPE 18

3.1 Problem identification 18

3.2 Research objectives 18

3.3 Relation to the journal article ... 19

CHAPTER 4 COMPLEMENTARY DEVELOPMENTS SUPPORTING MULTINOZZLE ARCHITECTURE ... 20

4.1 Development Context and Overview of the Printing Platform ... 20

4.2 Preliminary Concept Using Assembled Commercial Tapered Tips ... 21

4.3 Manufacturing Strategy for a Replaceable Tapered Array ... 23

4.4 Post-Extrusion Microstructural State of EC3515-10%FS ... 25

4.5 Supporting Digital Developments ... 27

4.5.1 Extension of the MEPM for Tapered Nozzles ... 27

4.5.2 Extension of the MTG ... 27

4.6 Chapter Summary ... 28

CHAPTER 5 ARTICLE 1: ADDITIVELY MANUFACTURED TAPERED MULTINOZZLE ARCHITECTURE FOR HIGH-FLOW DIRECT INK WRITING OF HIGHLY VISCOUS THERMOSET COMPOSITES ... 29

5.1 Introduction ... 30

5.2 Methods and Materials ... 31

5.2.1 Overview of the DIW Platform ... 31

5.2.2 Materials ... 33

5.2.3 Printing protocol and toolpath execution ... 34

5.2.4 Characterization ... 35

5.2.5 Fluid Modeling ... 37

5.3 Tapered Multinozzle Architecture: Design, Fabrication, and Characterization ... 37

5.3.1 Existing Multinozzle Architectures and Practical Design Constraints ... 37

5.3.2 Grid-Based Parallelization Strategy for Scaffold Fabrication ... 39

5.3.3 Channel Geometry and Hydraulic Design ... 42

5.3.4 Final Nozzle Geometry Selection ... 45

5.3.5 Printhead Fabrication and Dimensional Characterization ... 47

5.3.6 Position within the DIW Printhead Flow Rate-Outlet Diameter Design Space ... 48

5.4 Printing Demonstration and Fidelity Assessment ... 51

5.4.1 Experimental Pressure-Speed response across three material systems ... 51

5.4.2 Printed Microscaffold Across Material Systems 53
5.4.3 Geometric Fidelity of the Printed EC3515-10%FS Microscaffold 56
5.5 Conclusion 59
CHAPTER 6 CONCLUSION AND RECOMMENDATIONS 61
6.1 Summary of Work 61
6.2 Limitations 62
6.3 Recommendations for Future Work 63
6.4 Project Significance 64
REFERENCES 65
APPENDICES 71

LIST OF TABLES

Table 2.1: Representative multinozzle architectures reported in DIW 12

Table 2.2: Subtractive microfabrication routes for micro-scale components (compiled from [62], [64], [65]). 13

Table 2.3: Additive microfabrication routes for micro-scale components (adapted from [66]). .. 14

Table 5.1: Geometric and fabrication characteristics of representative DIW nozzle architectures 38

Table 5.2: Summary of printing conditions and geometric characteristics of microscaffolds fabricated using the tapered multinozzle. 53

LIST OF FIGURES

Figure 1.1: Project context and main constraints motivating the present work. (A) Representative porous microscaffold architecture targeted within the FACMO program. (B) First-generation 26-nozzle cylindrical multinozzle developed during FACMO1. (C) 50 cc and 250 cc reservoir used in the robotic DIW platform. (D) SEM image of extruded filament through a 250 µm diameter cylindrical nozzle, showing hollow glass microsphere crushing [9]. 2

Figure 2.1: Representative examples from the literature of custom nozzle geometries fabricated by stereolithography for DIW and related extrusion-based printing: (A) chaotic-printing nozzle with internal mixing elements; (B) coaxial extrusion nozzle; (C) multicore-shell coextrusion nozzle; (D) multimaterial 1D and 2D nozzle arrays; and (E) rotating multimaterial nozzle for helicoidal filament structuring. Adapted from [58], [67], [68], [69], [70]. 16

Figure 4.1: Photograph of the LM^2 robotic DIW platform 20

Figure 4.2: Preliminary multinozzle prototype based on commercial tapered dispensing tips. a) Custom trimming jig composed of a two-part FFF-printed body and a sliding razor-blade carriage, used to position and cut tapered tips. b) Representative trimmed commercial tapered tip. c) Compact manifold with stainless-steel tube inserts bonded into the body to provide leak-tight seats for the truncated tips. d) Assembled 5 × 5 prototype (N = 25) illustrating the packing density achievable with shortened tips. e) Benchtop extrusion setup mounted on the Aerotech system, including syringe, piston, pressure inlet, clamp, and installed multinozzle. f) Organic ink microscaffold printed with 2 passes per layer of 5 × 5 multinozzle. g) Enlarged view of the printed structure, showing an average filament diameter d = 424 µm and average pore size p = 231 µm.. 23

Figure 4.3: Retained printhead assembly and fabrication strategy. (a) Close-up of the final outlet region mounted at the end of the reservoir, showing the SLA-fabricated multinozzle array and the titanium backing plate above a microscaffold printed with the final 36-nozzle architecture. (b) Cross-sectional view of a sectioned SLA array assembled with the backing plate, showing the tapered channels fully defined within the printed component. The figure highlights the

separation between the replaceable SLA-defined flow path and the reusable metallic structural support. 24

Figure 4.4: Post-extrusion microstructural state of EC3515-10%FS after curing inside the nozzle following printing. (A) Representative μCT slice and corresponding segmentation sequence showing the continuous matrix phase, intact glass bubbles, porosity, and fractured-bubble debris. (B) Magnified views of the segmented phases highlighting the morphology of preserved bubbles, irregular voids, and angular glass fragments. The figure shows that the post-extrusion material contains both intact and damaged hollow glass bubbles, indicating partial rather than uniform filler degradation. 26

Figure 5.1: (A) DIW platform comprising a six-axis robotic arm and a custom piston-driven hydraulic extrusion unit capable of pressures up to 20 MPa; the perspective view is adjusted for clarity and is not to scale. (B) Tapered multinozzle printhead integrating the nozzles within a single polymer component. (C) Schematic of a 2×2 grid multinozzle deposition kinematics showing simultaneous extrusion of parallel filaments along the printing direction. (D) Representative orthogonal porous microscaffold geometry used to evaluate the performance of the present multinozzle design, with a nominal filament diameter of 350 μm, in-plane spacing of 1 mm, and desired stacking height of 5.6 mm. 33

Figure 5.2: Grid-based parallelization strategy and build-rate scaling. (A) Retained multinozzle layout and filament-spacing geometry for three representative square grids: (i) $N = 4$, (ii) $N = 16$, and (iii) $N = 36$. (B) Estimated fabrication time for a representative planar structure (6.2 m × 78 mm × 5.6 mm) as a function of nozzle count at deposition speeds between 50 and 500 mm $s - 1$. Insets highlight the reduced influence of deposition speed at high nozzle count. 41

Figure 5.3: Finite-element prediction of flow behavior in cylindrical and tapered nozzle geometries.(A) Predicted extrusion pressure as a function of outlet velocity for cylindrical and tapered channels with outlet diameters ranging from 100 to 1000 μm and identical channel length (L = 17 mm). The red dashed horizontal line indicates the maximum available extrusion pressure of the system (20 MPa). (B) Predicted pressure–velocity relationships for taper half-angles ranging from 0° (cylindrical) to 8° for a fixed outlet diameter of 250 μm. (C) Simulated shear-rate distributions for cylindrical and 6° tapered channels (250 μm outlet diameter, L =

17 mm) at an outlet velocity of 100 mm s^{-1}. Full-channel views and outlet-region enlargements show that tapering confines the highest shear rates to a short region near the outlet, whereas elevated shear persists along most of the cylindrical channel. 44

Figure 5.4: (A) Optical microscope image of a representative 6 × 6 multinozzle array with nominal 230 μm outlet diameter, with a magnified view of a single row illustrating outlet size and aperture uniformity. (B) Measured outlet diameter distributions for multinozzle arrays with nominal outlet diameters of 230 μm and 350 μm, based on all 36 outlets per array; the 230 μm geometry was evaluated over 3 arrays (108 outlets total), and the 350 μm geometry over 12 arrays (432 outlets total). (C) SEM image of a representative 230 μm nozzle tip, showing aperture circularity and minor surface texture associated with the layer-wise SLA fabrication process. (D) Cross-sectional view of a longitudinally sectioned tapered channel used for internal surface roughness analysis, with the representative axial measurement region indicated; roughness was measured along the flow direction using multiple line traces and quantified as Ra, reported as mean ± standard deviation. 48

Figure 5.5: Predicted printhead total flow rate as a function of nozzle outlet diameter for different DIW nozzle architectures. For each architecture, the nozzle length is indicated by color using the scale on the right, and the marker pictogram represents nozzle count and layout. Solid lines show the predicted effect of varying nozzle outlet diameter for a fixed channel architecture. 51

Figure 5.6: Experimental pressure–speed response of cylindrical and tapered multinozzle geometries for three material systems. (A) Organic Ink, (B) EPON 828-14%FS thermosetting ink, (C) EC3515-10%FS composite ink. Circular markers denote cylindrical nozzles and triangular markers denote tapered nozzles. The red dashed horizontal line indicates the maximum available extrusion pressure (20 MPa). Panels (A–B) compare 0.25 mm tapered nozzles with the 0.25 mm cylindrical configuration of Chauvette et al. [13], whereas panel (C) compares a 0.35 mm tapered nozzle with a 1.50 mm cylindrical reference. 52

Figure 5.7: Printed microscaffolds obtained with the tapered multinozzle architecture across three material systems. (A) Top view of a 36 × 36 filament scaffold printed with the organic reference ink at 200 mm s^{-1}, with an enlarged region showing the local pore structure. (B) Top view of a scaffold printed with EPON 828–14%FS at 50 mm s^{-1}, showing interrupted

filaments and reduced local regularity. (C) Representative local view (blue zone) of a scaffold printed with EC3515-10%FS at 100 mm s^{-1}. (D) Larger view of the EC3515-10%FS scaffold, showing the full printed area and repeated multinozzle deposition pattern. (E) Cross-sectional view of the EC3515-10%FS scaffold, showing the stacked orthogonal filament architecture through 18 layers. 55

Figure 5.8: Geometric fidelity of the printed EC3515 microscaffold. (A) Comparison between the nominal and printed scaffold geometry: (i) CAD model, (ii) photograph of the printed scaffold used for µCT analysis, and (iii) C2M signed-distance deviation map between the µCT reconstruction and the CAD geometry. (B) Selected slices of the C2M map showing local deviation patterns in the upper and lower portions of the scaffold: (i) top-view slice from the upper region (ii), (iii) top-view slice from the bottom region (iv). (C) Histogram of C2M signed distances, also used as the color scale for the deviation maps, showing a mean signed deviation of +20.0 µm and a 90% central interval of −89.7 to +126.0 µm. (D) SEM images of the same scaffold sample at increasing magnification, showing the surface morphology of the extruded filaments. 58

LIST OF SYMBOLS AND ABBREVIATIONS

α	half-angle of the tapered channel
AM	additive manufacturing
CAD	computer-aided design
C2M	cloud-to-mesh
D	channel diameter
ΔP	pressure drop
η	apparent viscosity
D_{in}	inlet diameter
D_{out}	outlet diameter
DIW	direct ink writing
DLP	digital light processing
ECM	electrochemical machining
EDM	electro-discharge machining
FFF	fused filament fabrication
FS	fumed silica
$\dot{\gamma}$	shear rate
K	consistency index
L	channel length
λ_c	cutoff wavelength of the profile filter
LM_2	Laboratory for Multiscale Mechanics
MEPM	Multinozzle Extrusion Prediction Model
MTG	Multinozzle Toolpath Generator
μ	dynamic viscosity

μCT	X-ray micro-computed tomography
N	number of nozzles
p	center-to-center nozzle pitch
PMMA	polymethyl methacrylate
Q	volumetric flow rate
Q_i	volumetric flow contribution associated with geometry i
R	hydraulic resistance
R_i	hydraulic resistance associated with geometry i
R_a	arithmetic average roughness
RMS	root mean square residual error
SEM	scanning electron microscopy
SLA	stereolithography
SLM	selective laser melting
SLS	selective laser sintering
s	center-to-center filament spacing
TPP	two-photon polymerization
USM	ultrasonic machining

LIST OF APPENDICES

APPENDIX A EXTENSION OF THE MEPM TO TAPERED GEOMETRIES 71

APPENDIX B EXTENSION OF THE MTG 73

CHAPTER 1 INTRODUCTION

1.1 Project Context

This master's project was carried out within the FACMO2 research program (*Fabrication additive de composites à matrice organique*). The program is an industrial collaboration between Safran Aircraft Engines, Dyze Design, and the Laboratory for Multiscale Mechanics (LM2) at Polytechnique Montréal. Within this framework, the broader objective was to develop additive manufacturing approaches capable of producing lightweight, high-resolution, multifunctional structures for aerospace applications, with particular interest in porous abradable coatings and acoustically functional micro-architectures. In this context, Direct Ink Writing (DIW) was retained as a promising route because it can deposit reactive materials into controlled filamentary architectures, including periodic porous networks that are difficult to obtain by conventional manufacturing methods [1], [2], [3]. Although this work was motivated by aerospace needs, the underlying manufacturing challenges are also relevant to other DIW applications involving scaffold-like periodic structures.

The industrial motivation for this work came from the need to manufacture porous multifunctional structures relevant to aircraft engine environments. On one hand, porous and micro-architected networks are attractive for acoustic control because their internal geometry can be tailored to influence dissipation and sound absorption [4], [5], [6], [7]. On the other hand, abradable seal coatings are key engine components because they allow small blade-tip clearances while limiting blade wear, thereby contributing directly to engine efficiency [8]. Bringing these functions together motivates the development of low-density porous thermosetting structures inspired by acoustic microscaffolds, but adapted to the constraints of aerospace-grade abradable materials and representative component geometries [9], [10]. Figure 1.1 summarizes the project context and the main constraints that motivated the present work. Figure 1.1A shows a representative porous microscaffold architecture of the type achieved within FACMO1 using a single nozzle. For the industrial partner, the challenge was therefore not simply to print porous samples in the laboratory, but to move toward manufacturing strategies compatible with higher productivity, lower density, multifunctionality, and realistic material systems.

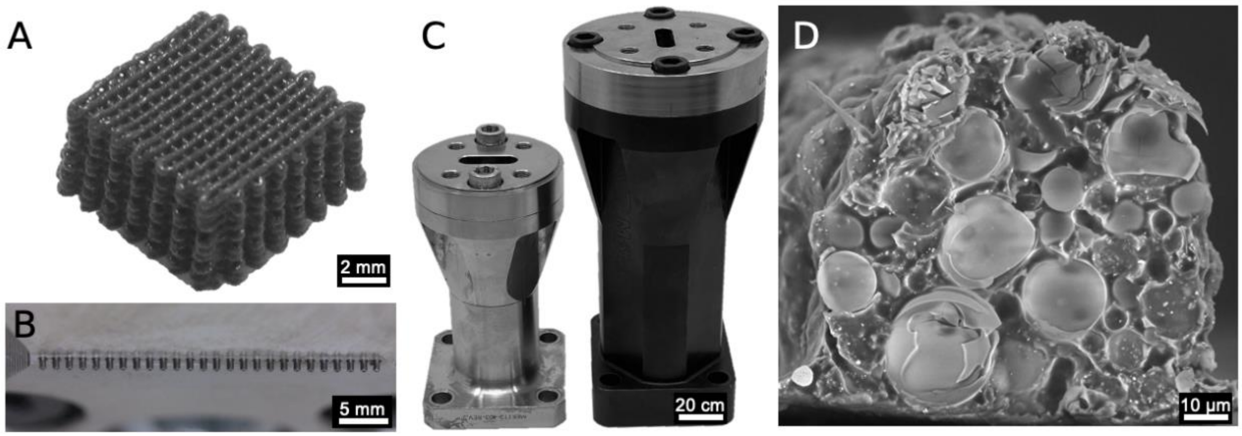

Figure 1.1: Project context and main constraints motivating the present work. (A) Representative porous microscaffold architecture targeted within the FACMO program. (B) First-generation 26-nozzle cylindrical multinozzle developed during FACMO1. (C) 50 cc and 250 cc reservoir used in the robotic DIW platform. (D) SEM image of extruded filament through a 250 µm diameter cylindrical nozzle, showing hollow glass microsphere crushing [9].

Previous work completed during FACMO1 had already established an important foundation. A high-pressure robotic DIW platform was developed at LM2 using a six-axis industrial robot coupled to a piston-driven extrusion system, together with dedicated digital tools for multinozzle pressure prediction and non-planar toolpath generation [10]. This first phase demonstrated the feasibility of multinozzle direct deposition for periodic porous structures, including high-speed printing of microscaffold-type architectures, curved-surface deposition, and the fabrication of representative demonstrators inspired by abradable seal coating applications [10]. Figure 1.1B presents the first-generation 26-nozzle cylindrical multinozzle developed during FACMO1. In parallel, complementary materials work showed that thermosetting abradable formulations could be tailored to become printable while preserving the low-density porous architectures required for acoustic functionality and abradability assessment [9]. Taken together, these studies confirmed the relevance of the robotic multinozzle DIW route and established that porous thermosetting micro-architectures could be manufactured in geometries of interest to the FACMO program.

However, these earlier successes also revealed a set of critical limitations. Although the first-generation cylindrical configuration enabled the first successful multinozzle demonstrations with the original high-pressure setup, its hydraulic resistance became a critical limitation once the extrusion system was reconfigured to process larger material volumes. Here, hydraulic resistance refers to the opposition of the internal flow path to material transport, whereas pressure drop refers to the pressure required to overcome that resistance at a given flow rate. Figure 1.1C presents the transition from the 50 cc to the 250 cc reservoir configuration, which increased the piston diameter and reduced the maximum available pressure from 65 MPa to 20 MPa. Under this new pressure limit, the pressure drop associated with the cylindrical nozzle architecture significantly restricted the accessible operating window. In parallel, the processing of low-density abradable formulations containing hollow glass microspheres revealed another limitation of the system, namely particle crushing during extrusion. This phenomenon is illustrated in Figure 1.1D through a representative SEM observation of fractured microspheres after extrusion [9], [10], [11], [12]. Finally, the cleaning procedure required between prints was meticulous and time-consuming, and insufficient cleaning could directly affect subsequent print quality. Together, these observations showed that the process concept had been validated, but that the printhead architecture had become a bottleneck in the transition toward more demanding materials and more representative operating conditions.

From the industrial perspective, this bottleneck became particularly important as the project moved toward more representative manufacturing conditions. Safran's needs pointed toward porous structures combining low density, abradability, and acoustic functionality, while also requiring higher productivity and materials closer to the targeted industrial system [9], [10]. In practical terms, this meant that the existing multinozzle strategy had to become more pressure-efficient without sacrificing outlet diameter, architectural compactness, or compatibility with the existing robotic extrusion platform. The hardware also had to remain realistic from a maintenance and replacement standpoint under the use of reactive filled thermosetting materials. These needs framed the specific gap addressed in this thesis: although FACMO1 had demonstrated robotic multinozzle DIW of porous thermosetting structures, a compact tapered multinozzle architecture adapted to pressure-limited extrusion of highly viscous abradable materials had not yet been developed or validated within the FACMO platform.

The present master's project was therefore defined to address that gap. Its role within FACMO2 was to redesign the multinozzle printhead, not to rebuild the entire robotic process from the ground up. More specifically, this work focused on the design, fabrication, integration, and evaluation of a new-generation multinozzle architecture intended for highly viscous abradable thermosetting materials. Within this scope, the present contribution is to translate the limitations identified in FACMO1 into concrete printhead design criteria, develop and fabricate a new tapered multinozzle concept compatible with the LM2 extrusion hardware, and assess its ability to support representative porous printing conditions for a more demanding material system. In that sense, this thesis occupies a precise position in the continuity of the FACMO program: it builds directly on the process, materials, and robotic foundations established previously, while targeting the printhead-scale limitation that prevented further progress toward more representative industrial conditions.

1.2 Research Objectives

The general objective of this project is to develop and demonstrate the feasibility of a new-generation tapered multinozzle architecture for the Direct Ink Writing of highly viscous abradable thermosetting materials under the pressure limitations of the existing LM2 robotic extrusion platform.:

I. Design, fabricate, and integrate a tapered multinozzle printhead compatible with the existing high-pressure robotic DIW system.
II. Evaluate the hydraulic behavior and printing feasibility of the developed printhead through the fabrication of representative porous microscaffold structures.

1.3 Thesis Outline

This thesis consists of six chapters. Chapter 1 is the introduction, including the project context and research objectives. Chapter 2 is the literature review. Chapter 3 is the problem statement and the position of the submitted article within the thesis. Chapter 4 is the complementary engineering work associated with the proposed multinozzle architecture. Chapter 5 is the submitted scientific article, entitled *Tapered Multinozzle Architecture for High-Flow Direct Ink Writing of Highly Viscous Thermoset Composites*. Chapter 6 is the general conclusion and recommendations for future work.

CHAPTER 2 LITERATURE REVIEW

2.1 Additive Manufacturing and the Place of Direct Ink Writing

Additive manufacturing (AM) encompasses a broad class of processes in which three-dimensional components are built layer by layer directly from digital models. Depending on the underlying material transformation mechanism, AM processes may rely on polymer melting and solidification, powder-bed fusion or binding, vat photopolymerization, or the deposition of pastes, suspensions, and inks [13], [14]. This manufacturing paradigm has attracted strong research and industrial interest because it enables the fabrication of geometrically complex and customized parts while reducing tooling constraints and facilitating rapid design iteration [13], [15]. Within this broader landscape, extrusion-based approaches occupy an important position for the processing of materials that are not readily compatible with melting- or sintering-based routes.

Direct Ink Writing (DIW) is a material-extrusion AM technique in which an ink is extruded through a nozzle and deposited in a programmed path to form three-dimensional structures layer by layer [16], [17], [18]. In contrast to thermally driven extrusion processes, DIW generally operates at or near room temperature and is compatible with a wide range of materials, including hydrogels, elastomers, ceramics, thermosetting polymers, and particle-filled composites [14], [15], [19]. This broad material compatibility has supported the development of DIW across diverse applications such as biomedical scaffolds, soft and multifunctional structures, architected lattices, and composite materials with tailored mechanical or functional performance [3], [15], [18], [20].

A defining characteristic of DIW is that processability is governed primarily by ink rheology rather than by phase change. During extrusion, the material must flow through the nozzle under shear, while after deposition it must recover sufficient resistance to deformation to retain its shape and support subsequent layers [14], [19], [21]. The ability of DIW to process such a wide range of formulations therefore arises not from a universal thermal cycle, but from the possibility of tailoring ink behavior to satisfy both flow and shape-retention requirements. This rheology-driven character distinguishes DIW from many other AM processes and makes it especially attractive for materials whose functional properties depend on composition, filler loading, or curing chemistry.

2.2 Rheology and Printability in DIW

Because Direct Ink Writing relies on the extrusion of a formulated ink through a confined nozzle followed by deposition in open air or onto a substrate, printability is governed primarily by rheological behavior rather than by a universal thermal cycle. Depending on the material system, printable DIW inks may exhibit combinations of shear-thinning behavior, apparent yield stress, viscoelasticity, thixotropy, or other forms of structural recovery that enable flow during extrusion while limiting deformation after deposition [14], [19], [22]. No single rheological signature defines all DIW inks. Instead, successful formulations must satisfy two partially competing requirements: sufficiently low resistance to flow under printing conditions and sufficient stability after deposition to preserve the intended geometry [15], [21], [23].

To describe these behaviors, DIW inks are often represented using constitutive models of varying complexity depending on the material and the intended analysis. Generalized Newtonian formulations such as the power-law, Herschel–Bulkley, and Bingham-type models are commonly used to capture shear-thinning behavior and, where relevant, the onset of flow through an apparent yield stress [22], [24], [25], [26]. In some cases, Carreau-type models may also be employed when a broader shear-rate range must be represented. These approaches are useful for describing extrusion behavior and comparing formulations, although they do not necessarily capture all aspects of structural recovery, viscoelasticity, or time-dependent evolution in more complex inks [25], [27].

Among the rheological features most frequently associated with DIW, shear thinning is particularly important because it allows viscosity to decrease under the high shear conditions encountered within the nozzle, thereby facilitating extrusion [14], [19], [22]. After deposition, however, the material must resist spreading, sagging, or collapse. This stability may arise from different mechanisms depending on the formulation, including yield-stress behavior, elastic response, particle-network interactions, or rapid structural rebuilding at rest [23], [25], [27]. Thixotropy refers to a reversible decrease in viscosity under shear followed by progressive structural recovery at rest, and is therefore often advantageous in DIW because it supports repeated flow–recovery cycles during printing [22], [28], [29].

Overall, the rheological requirements of DIW are best understood as material- and application-dependent rather than universal. Hydrogels, ceramic pastes, particle-filled suspensions, elastomeric inks, and curable polymers may all be printable by DIW, but they do not rely on exactly the same stabilization mechanisms [3], [14], [15], [19], [20]. What these systems share is the need for a controlled balance between flowability during extrusion and resistance to deformation after deposition. This general framework provides the basis for the following section, which narrows the discussion to highly viscous, filled, and thermosetting inks, where extrusion constraints increasingly shift from post-deposition shape retention toward nozzle-scale flow resistance and time-dependent process stability.

2.3 Extrusion of Highly Viscous, Filled, and Thermosetting Inks

As ink viscosity and geometric confinement increase in Direct Ink Writing, extrusion progressively shifts into a regime in which process feasibility is governed less by post-deposition shape retention than by the ability of the system to force material through the nozzle. Because DIW generally operates at very low Reynolds numbers, inertial effects are typically negligible and pressure losses are dominated by viscous dissipation [11], [24], [26]. Under these conditions, the pressure required to sustain a given flow rate depends strongly on both material rheology and flow-path geometry. For non-Newtonian inks commonly encountered in DIW, the pressure-flow relationship is generally nonlinear because the apparent viscosity evolves with shear rate. In many shear-thinning systems, this behavior partly mitigates the pressure increase associated with higher flow rates. However, when the ink remains highly viscous and is extruded through strongly confined geometries, the required pressure can still rise rapidly and approach hardware limits [22], [30]. As a result, highly viscous inks do not simply represent a more difficult version of conventional DIW formulations; they can place the process in a fundamentally pressure-limited operating regime.

This transition is especially important for particle-filled systems. Increasing solids loading generally raises apparent viscosity, can increase apparent yield stress, and may introduce additional flow heterogeneity through particle-particle and particle-wall interactions [12], [21], [31], [32]. In practice, these effects narrow the operating window by increasing extrusion resistance and sensitivity to nozzle dimensions, internal surface condition, and geometric discontinuities. For highly filled systems, the ability to initiate extrusion may therefore become limited not only by the formulation itself, but also by the maximum pressure that the hardware can generate and sustain. In this context, throughput can no longer be increased freely by raising extrusion rate, since the required pressure may exceed system limits before the desired deposition speed is reached [11], [22], [33].

Thermosetting inks constitute a particularly constrained subclass within this broader regime. Unlike thermoplastics, which may be repeatedly softened and resolidified, thermosetting polymers undergo irreversible crosslinking during curing, progressively increasing viscosity and eventually forming a permanent network [34], [35]. In DIW, this means that rheological properties may evolve over timescales comparable to the print itself, leading to a continuous drift in extrusion conditions during deposition. Rheology modifiers such as fumed silica or organoclays are often introduced to improve shape retention and induce shear-thinning or yield-like behavior, but they also tend to increase low-shear viscosity and further amplify pressure demand [14], [22]. When particulate fillers are added on top of a reactive matrix, the combined effects of high viscosity, solids loading, and time-dependent curing can make stable extrusion particularly sensitive to nozzle-scale flow resistance.

This behavior differs in an important way from that of physically structured inks exhibiting reversible thixotropic recovery. In such systems, shear history and rest time may be used to temporarily fluidize the material and then rebuild structure after deposition. In thermosetting systems, by contrast, viscosity growth is driven at least in part by irreversible chemical reactions rather than by reversible structural rebuilding alone [29], [36], [37]. The printable window therefore tends to contract as processing time increases, reducing tolerance to long print durations, recirculation, or repeated conditioning. From an application standpoint, this is especially relevant for industrial thermosetting composites, which are attractive because of their thermal stability, dimensional robustness, and functional performance, but are often substantially more difficult to extrude than softer or less concentrated DIW inks [13], [31].

Taken together, these considerations indicate that highly viscous, filled, and thermosetting inks should not be viewed only through the lens of general DIW printability. In this regime, extrusion feasibility is governed increasingly by the interaction between material rheology, time-dependent process stability, and nozzle-scale hydraulic resistance. This shift in constraint motivates closer attention to flow-path design, and in particular to how nozzle geometry can be used to reduce pressure demand without sacrificing deposition scale.

2.4 Nozzle Geometry and Hydraulic Resistance in DIW

In DIW, the nozzle is the most restrictive element of the extrusion system and therefore exerts a strong influence on the pressure required to sustain a given flow rate. More generally, pressure loss in confined internal flows depends on both fluid rheology and geometric factors such as channel length, cross-sectional dimensions, contraction profile, and local singularities associated with entrances, exits, and abrupt changes in section [30], [38], [39]. In DIW, where inks are often highly viscous and the characteristic dimensions of the flow path are small, these geometric effects become especially important. Under such conditions, nozzle design should not be viewed merely as a means of defining filament diameter, but also as a primary determinant of extrusion pressure and process feasibility.

Much of the DIW literature nevertheless relies, either explicitly or implicitly, on cylindrical nozzles as a practical baseline. This choice is understandable, since commercially available dispensing tips and simple capillary geometries are easy to integrate and characterize. For laminar flow of a Newtonian fluid in a cylindrical capillary, the Hagen–Poiseuille relation gives

$$\Delta P = \frac{128\mu L Q}{\pi D^4} \quad (2.1)$$

where ΔP is the pressure drop, μ the viscosity, L the nozzle length, Q the volumetric flow rate, and D the internal diameter. Although many DIW inks are non-Newtonian, this classical result remains useful as a first-order illustration of the strong dependence of pressure drop on geometric confinement, particularly the inverse fourth-power dependence on diameter [30]. Cylindrical channels maintain the minimum cross-section over the full nozzle length, which increases viscous dissipation and can impose a strong hydraulic penalty when outlet diameters are reduced or when highly viscous inks are processed. Analytical and experimental studies of ink extrusion confirm that pressure demand is highly sensitive to nozzle dimensions, with channel diameter and length exerting a particularly strong influence on the pressure-flow relationship [24], [40], [41]. As a result, nozzle geometry becomes a critical design variable once DIW enters a pressure-limited operating regime.

Within this broader context, converging or tapered channels are of particular interest because they allow the material to progressively contract toward the outlet rather than remaining confined to the minimum diameter along the entire flow path. Studies in extrusion, die design, and related nozzle-driven processes have shown that such geometries can reduce pressure losses relative to straight cylindrical channels of identical outlet size, while also modifying the internal distribution of shear and extensional deformation [41], [42], [43], [44]. Recent work in extrusion-based additive manufacturing has similarly emphasized that nozzle profile can be treated as an explicit design variable rather than a fixed hardware constraint, with optimized or customized nozzle shapes offering a route to improved flow behavior and printability [45], [46]. In DIW specifically, this is attractive because it offers a possible means of reducing pressure demand without increasing outlet diameter and therefore without directly sacrificing deposition scale.

For printheads comprising multiple outlets, the hydraulic problem extends beyond the local nozzle profile to include flow distribution across the manifold feeding the channels. Uniform flow among parallel outlets is a classical challenge in manifold design, since even small differences in path resistance can lead to unequal outlet flow rates and therefore non-uniform deposition [47], [48], [49], [50]. Similar issues arise in additive manufacturing printheads and multi-flow devices, where channel layout and manifold design strongly affect balancing performance and practical scalability [51], [52], [53]. In DIW, these considerations imply that improving throughput is not only a question of increasing material feed, but also of controlling nozzle-scale resistance and, in architectures using multiple outlets, flow distribution across the printhead. This provides the basis for the next section, which examines multinozzle architectures as a strategy for throughput scaling in DIW.

2.5 Multinozzle Architecture in DIW

When single-nozzle Direct Ink Writing becomes too slow for the fabrication of large areas or repeated filament networks, one possible response is to distribute material delivery across several outlets operating simultaneously. In such configurations, the total deposited volume can be increased without requiring each individual nozzle to carry the full material flow associated with the target build rate. Multinozzle architectures are therefore of interest when fine filament dimensions must be maintained while reducing fabrication time over large areas or repeated patterns [54], [55], [56]. This approach has been explored in DIW for applications including microvascular-style printing, multimaterial deposition, repeated part replication, and architected scaffold fabrication [54], [55], [56], [57], [58], [59].

Representative multinozzle architectures reported in the DIW literature are presented in Table 2.1 as a visual overview of the main design approaches found in the field. These studies show that multinozzle DIW systems can be grouped into several broad architectural families. Branched manifold architectures distribute material from one or more inlets through internal channels toward multiple outlets, as illustrated by the systems of Hansen et al. (2013), Skylar-Scott et al. (2019), and Weiss et al. (2025). In contrast, direct-feed endplate architectures integrate the nozzles directly into the perforated end of a common pressurized reservoir, as in the work of Chauvette et al. (2021, 2023). A third category is formed by connector-fed architectures, in which each nozzle is supplied through an individual connection or assembled feed path, enabling modularity and, in some cases, straightforward multimaterial integration, as reported by Uzel et al. (2022) and Al-Ali and Almubarak (2025).

Taken together, these studies show that multinozzle DIW systems have been developed for different objectives and under different design constraints. Some emphasize dense parallel deposition from a single material source, whereas others prioritize multimaterial capability, substrate conformity, modularity, or low-cost implementation. They also differ substantially in fabrication route, ranging from machined rigid components to stereolithography-fabricated manifolds and assembled connector-based systems. Nevertheless, across these reported architectures, individual channels are still most often cylindrical or inherited directly from commercially available dispensing components. As a result, the internal nozzle profile is rarely treated as a hydraulic design variable.

This point is particularly important for highly viscous and particle-filled inks. While adding outlets can reduce fabrication time, it does not by itself remove the pressure required to drive material through each nozzle. The practical benefit of multinozzle deposition therefore remains strongly linked to the hydraulic resistance of the local flow path, as well as to the ability of the printhead to distribute material uniformly across the array. For highly viscous thermosetting systems, multinozzle design must therefore address not only outlet count and spatial arrangement, but also channel geometry, flow balancing, structural robustness, and fabrication practicality. These combined constraints motivate the examination of manufacturing routes for multinozzle printheads, which is discussed in the following section.

Table 2.1: Representative multinozzle architectures reported in DIW

Authors	Highlights	Image	Reference
Hansen et al., 2013	• Branched manifold architecture • 64 outlets, 200 µm diameter • Machined PMMA • Mechanical pressure actuation • Single material, reduced fabrication time	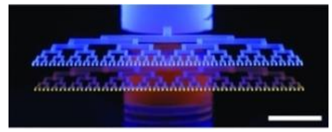	[55]
Skylar-Scott et al., 2019	• Branched manifold architecture • 1 -128 outlets, 1D and 2D array • SLA-fabricated • Pneumatic pressure actuation • Multimaterial, voxelated deposition	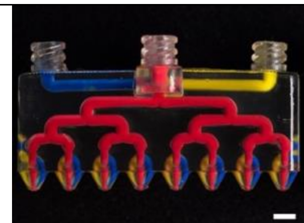	[58]
Chauvette et al., 2021-2023	• Direct-feed endplate architecture • 26 outlets, 250 µm diameter • Machined metallic • Mechanical pressure actuation • Single material, reduced fabrication time		[54], [60], [61]
Uzel et al., 2022	• Connector-fed architecture • 16 outlets, 1.37 mm diameter • Multi-component assembly • Independent vertical compliance • Pneumatic pressure actuation • Multimaterial, non-planar substrates	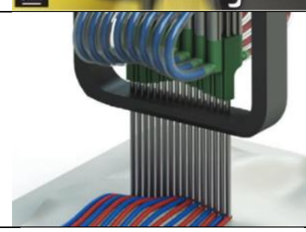	[56]
Weiss et al., 2025	• Branched manifold architecture • Up to 32 outlets • FFF manifold with Luer-lock nozzles • Pneumatic pressure actuation • Low-cost and open source • Single material, replicated part production	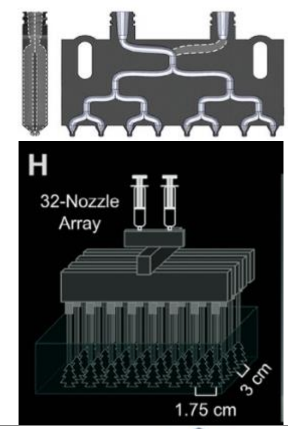	[59]
Al-Ali et al., 2025	• Connector-fed modular architecture • Up to 10 outlets, 5 demonstrated • Bent Luer-lock nozzles • Pneumatic pressure actuation • Multimaterial, compact layout	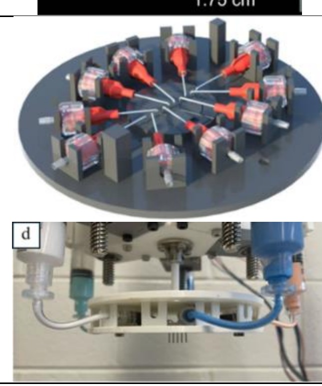	[57]

2.6 Manufacturing Routes for Multinozzle Printheads

For multinozzle DIW printheads, the fabrication route is not only a manufacturing choice but also a design constraint. Dense arrays must integrate multiple small internal flow paths within a limited footprint while maintaining dimensional repeatability, sufficient structural integrity, and compatibility with the targeted ink system. These requirements become more demanding when the printhead is intended for highly viscous or reactive materials. In such cases, pressure resistance and cleaning become more critical, and iterative refinement of the geometry is often required during development.

Conventional subtractive microfabrication methods remain relevant when rigid, pressure-resistant components are required. As summarized in Table 2.2, processes such as micromilling, laser micromachining, EDM, ECM, and ultrasonic machining can achieve small features with useful dimensional control and, in some cases, favorable surface quality, but they are generally constrained by tool accessibility, material compatibility, feature aspect ratio, or sequential fabrication time [62], [63], [64], [65]. These limitations become increasingly important for dense multinozzle arrays, where repeated internal features must be produced with consistent spacing and geometry.

Table 2.2: Subtractive microfabrication routes for micro-scale components (compiled from [62], [64], [65])

Process	Typical min feature size (µm)	Typical Aspect Ratio	Typical Wall Roughness (µm)	Material classes
Micromilling	10-50	10-50	~0.2-2	Metals, polymers, ceramics
Laser micromachining	1-10	1-10	~0.1-2	Metals, polymers, ceramics, glass
Electro-discharge machining (EDM)	5-25	10-100	~0.1	Electrically conductive
Electrochemical machining (ECM)	0.2-5	<10	<0.1	Electrically conductive

Ultrasonic machining (USM)	5	<7	-	Hard and brittle

Additive fabrication routes offer greater geometric freedom by enabling internal channel networks to be produced directly within a monolithic part. Table 2.3 summarizes representative additive microfabrication methods in terms of achievable resolution, representative build area, material class, and principal process constraints [13], [66]. Among these methods, photopolymerization-based processes such as stereolithography are particularly attractive for multinozzle printheads because they combine adequate resolution with relatively large build size and rapid design iteration. Other additive methods may offer advantages in specific contexts, but often with trade-offs in surface quality, material choice, or internal channel accessibility.

Table 2.3: Additive microfabrication routes for micro-scale components (adapted from [66])

Process	**Resolution (µm)**	**Representative Build Area (mm^2)**	**Material Classes**	**Process constraint**
TPP	0.08 - 0.26	0.0001 - 12.25	Photopolymer	Extremely limited build volume and low fabrication rate
DLP	0.6 - 65	2 - 8761	Photopolymer	Pixel-size-limited lateral resolution; Internal resin evacuation constraints
SLA	75 - 200	[21 – 1 140] x 10^3	Photopolymer	Resolution-fabrication rate trade-off; Internal resin evacuation constraints
DIW	150 – 50 000	900 – 100 x 10^6	Polymers, ceramics, composites	Nozzle-diameter and rheology-limited feature size; material-dependent consolidation
Inkjet	34 - 85	[52 – 800] x 10^3	Photopolymers	Droplet coalescence, spreading, and curing constraints

FFF	127 - 1000	[64 – 1 010] x 10^3	Thermoplastics	Nozzle-diameter-limited feature size and interlayer bonding constraints
SLS / SLM	55 - 500	[9.6 – 250] x 10^3	Polymers (SLS), Metals (SLM)	Powder evacuation from enclosed features; roughness and thermal distortion constraints

Beyond these general comparisons, Figure 2.1 presents representative examples from the literature of custom nozzle geometries fabricated by stereolithography for DIW and related extrusion-based printing. These studies do not address the same hydraulic objective as the present work, but they show that SLA can produce functional nozzle architectures with enclosed internal channels, multiple inlets, and compact multichannel routing features that would be difficult to realize by conventional machining.

The examples gathered in Figure 2.1 illustrate several distinct uses of SLA-fabricated nozzle design. Figure 2.1A shows the chaotic-printing nozzle of [67], in which four inlets and internal mixing elements progressively reorganize the material streams before extrusion. Figure 2.1B and Figure 2.1C show that SLA is also used to fabricate coaxial and multicore-shell nozzles with controlled internal compartmentalization for coextrusion [68], [69]. Figure 2.1D extends this logic to 1D and 2D multimaterial nozzle arrays with integrated internal routing [58], while Figure 2.1E shows a rotating nozzle whose internal geometry directly governs the helicoidal organization of the deposited filament [70]. Taken together, these examples confirm that SLA is already an established route for the fabrication of customized functional nozzle geometries. From a practical standpoint, operation and maintenance are also important selection criteria. For printheads used with filled or thermosetting inks, residual material inside narrow channels can complicate cleaning and reduce repeatability during reuse [71]. In this context, low-cost additive fabrication can support not only rapid prototyping, but also replaceable or semi-disposable architectures when maintenance becomes impractical. This consideration is particularly relevant for compact multinozzle systems, where cleaning each internal path individually may be difficult once reactive material has partially cured.

Taken together, Tables 2.2 and 2.3 and Figure 2.1 show that no single fabrication route simultaneously maximizes geometric precision, material flexibility, design freedom, pressure resistance, and ease of replacement. Subtractive methods remain attractive for robust pressure-resistant parts, whereas additive routes, and especially SLA, offer clear advantages for producing compact monolithic geometries with complex internal flow paths. In the DIW literature, these capabilities are most often used for mixing, coextrusion, multimaterial routing, or filament structuring. In the present work, however, the same fabrication route is considered for a different purpose: producing a tapered multinozzle architecture intended to reduce hydraulic resistance under pressure-limited extrusion conditions for highly viscous thermosetting composites.

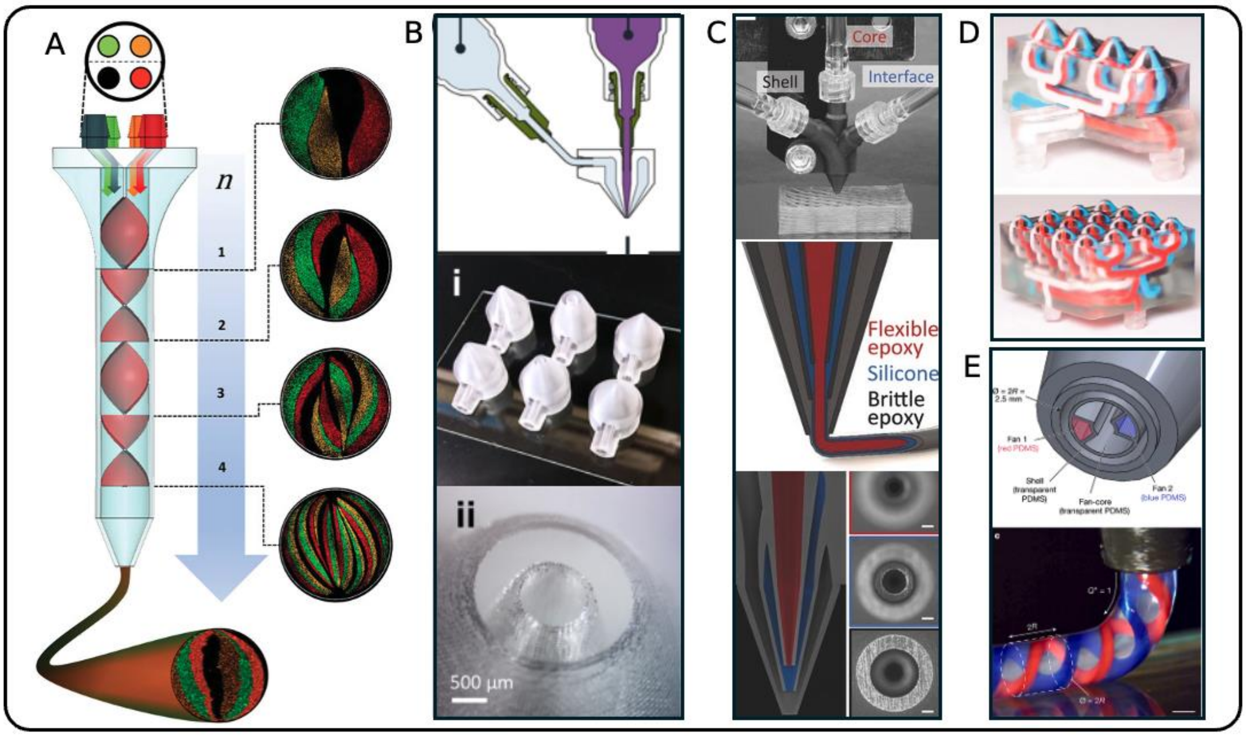

Figure 2.1: Representative examples from the literature of custom nozzle geometries fabricated by stereolithography for DIW and related extrusion-based printing: (A) chaotic-printing nozzle with internal mixing elements; (B) coaxial extrusion nozzle; (C) multicore-shell coextrusion nozzle; (D) multimaterial 1D and 2D nozzle arrays; and (E) rotating multimaterial nozzle for helicoidal filament structuring. Adapted from [58], [67], [68], [69], [70].

2.7 Synthesis and Research Gap

The literature reviewed in this chapter shows that Direct Ink Writing is a versatile additive manufacturing process for materials that cannot be readily processed through melting-based routes, including highly filled suspensions, curable polymers, and viscoelastic pastes. However, when ink viscosity and solids loading increase, DIW progressively shifts into a pressure-limited regime in which extrusion feasibility is governed less by deposition accuracy than by the ability of the system to overcome nozzle-scale hydraulic resistance. This constraint becomes even more severe for thermosetting systems, whose viscosity evolves irreversibly during curing and progressively narrows the printable processing window.

The review also highlights two complementary strategies for extending DIW toward this regime: reducing hydraulic resistance through internal nozzle design and increasing throughput through multinozzle parallelization. Converging or tapered channels have been shown to reduce pressure losses relative to cylindrical geometries, while multinozzle printheads enable higher total deposition rates without sacrificing filament-scale resolution. Yet these approaches have rarely been combined in compact architectures for highly viscous thermosetting materials. Most reported multinozzle DIW systems continue to rely on cylindrical channels, and the internal nozzle profile is seldom treated as a key hydraulic design variable.

In addition, dense multichannel printheads for reactive, particle-filled materials must satisfy practical constraints in fabrication, structural resistance, cleaning, and iteration cost. These combined limitations define the gap addressed in this thesis: the need for a compact and manufacturable multinozzle architecture that reduces pressure demand, preserves fine deposition, and remains operationally practical for highly viscous thermosetting composites.

CHAPTER 3 METHODOLOGY AND SCOPE

3.1 Problem identification

Multinozzle DIW using a 6-axis robotic platform shows strong potential for the fabrication of periodic structures for aerospace applications. However, the following issues need to be addressed:

- Current multinozzle printhead configurations remain limited to relatively low flow rates and moderate-viscosity materials.
- Most DIW systems rely on formulation adaptation to enable printability rather than on architectural modifications.
- Existing multinozzle designs are primarily developed for proof-of-concept or laboratory-scale demonstrations, with limited consideration for faster turnaround and practical printhead replacement.

3.2 Research objectives

The general objective of this project is to develop and demonstrate the feasibility of a new-generation tapered multinozzle architecture for the Direct Ink Writing of highly viscous abradable thermosetting materials under the pressure limitations of the existing LM2 robotic extrusion platform. The specific objectives are presented as follows:

I. **Design, fabricate, and integrate a tapered multinozzle printhead compatible with the existing high-pressure robotic DIW system.** The design is intended to reduce hydraulic resistance, enable the extrusion of highly viscous abradable thermosetting materials under pressure-limited conditions, and remain compatible with practical requirements related to printhead replacement and cleaning.

II. **Evaluate the hydraulic behavior and printing feasibility of the developed printhead through the fabrication of representative porous microscaffold structures.** This evaluation focuses on the pressure required to sustain extrusion, the stability of multinozzle deposition, and the feasibility of fabricating representative porous microscaffold structures under pressure-limited conditions.

3.3 Relation to the journal article

The main results of this research are presented in the form of a journal article reproduced in Chapter 5. Entitled *Tapered Multinozzle Architecture for High-Flow Direct Ink Writing of Highly Viscous Thermoset Composites*, this paper constitutes the principal outcome of the master's project and addresses the two research objectives stated in Section 3.2.

The article presents the design, fabrication, and experimental evaluation of a tapered multinozzle architecture for the DIW of highly viscous thermosetting composites under pressure-limited conditions. It shows that, compared with previously implemented cylindrical multinozzle configurations, the proposed architecture reduces hydraulic resistance and supports stable high-speed extrusion while preserving fine outlet dimensions compatible with representative porous microscaffold fabrication.

Within the thesis, the article forms the core scientific contribution, while the surrounding chapters provide the broader literature background, methodological framing, and complementary technical developments that could not be included in the journal format. The manuscript has been submitted to *Additive Manufacturing*.

Mr. Plante designed and performed the experiments, analyzed the data, and wrote the article under the supervision of Prof. Daniel Therriault and Prof. Sampada Bodkhe, with revisions by Dr. Farahani. Mr. Roussel contributed to the preparation and conduct of the experiments. Ms. Rozier contributed to the rheological study of the material and assisted with experimental preparation.

CHAPTER 4 COMPLEMENTARY DEVELOPMENTS SUPPORTING MULTINOZZLE ARCHITECTURE

4.1 Development Context and Overview of the Printing Platform

The developments presented in this chapter use the LM2 robotic Direct Ink Writing platform in its 250 cc configuration. Figure 4.1 shows the system used in the present work, including the FANUC robot, the hydraulic extrusion unit, the 250 cc reservoir, and the printhead mounted at the reservoir outlet. This platform defines the hardware framework within which the new multinozzle architecture is developed. The FANUC robot is retained for its ability to accommodate interchangeable deposition hardware, for its 25 kg payload, and for its compatibility with non-planar toolpaths previously developed within the FACMO program. Its large working envelope also places the present work within a manufacturing system intended for larger-scale deposition. Within this framework, the printhead must remain compatible with the existing extrusion hardware while preserving fine outlet dimensions suitable for representative porous microscaffold fabrication.

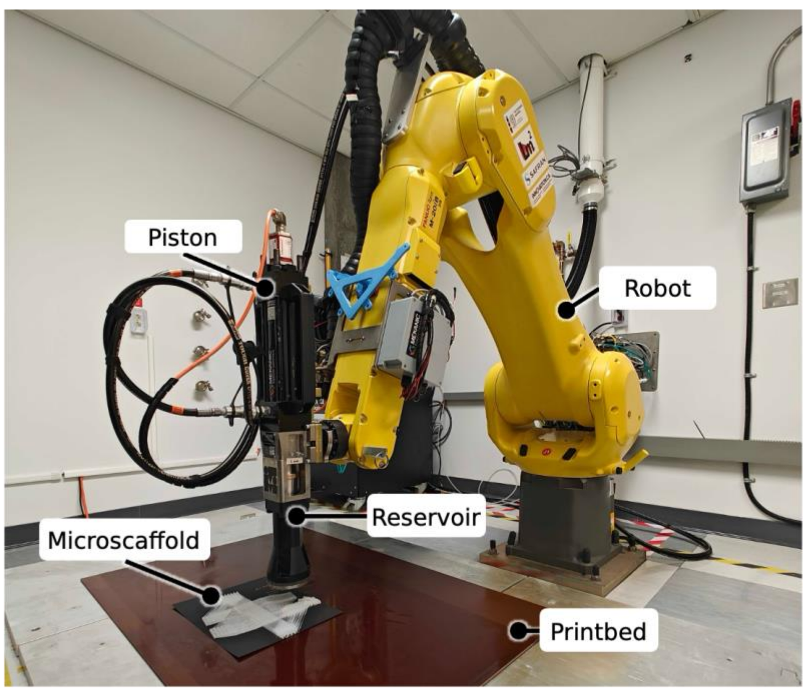

Figure 4.1: Photograph of the LM^2 robotic DIW platform

4.2 Preliminary Concept Using Assembled Commercial Tapered Tips

A preliminary 5 × 5 tapered multinozzle concept is assembled from modified commercial 0.41 mm dispensing tips. Figure 4.2 presents this design trial and the deposited pattern obtained from it. The concept examines whether off-the-shelf tapered nozzles can be adapted to the outlet of a larger reservoir, packed densely within that circular footprint, and used to deposit controlled parallel filaments in a microscaffold-type pattern.

Figure 4.2A shows the trimming jig used to shorten the commercial tips reproducibly. A tapered tip is inserted in the jig at a fixed depth, while a sliding razor-blade carriage guides the cut in a guillotine-like motion. This arrangement reduces human variability during trimming and makes the operation faster and safer than manual cutting with a box cutter. Figure 4.2B shows a representative trimmed tip. The modification preserves the 0.41 mm tapered outlet region while reducing the external base diameter from approximately 8 mm to 3 mm. This reduction is essential for increasing outlet density within the available footprint.

Figure 4.2C shows the custom manifold used to integrate the trimmed tips at the outlet of a larger reservoir. On the reservoir side, the manifold forms a short cylindrical adapter with a perforated cap that fits over the end of a 30 cc syringe after removal of the original syringe tip. On the outlet side, the same part contains 25 shouldered holes into which short stainless-steel tubes are bonded. These tubes reproduce a sealing action analogous to the original luer-lock connection by biting into the thermoplastic tapered tips. Figure 4.2D shows the assembled 5 × 5 prototype. A second perforated plate with chamfered holes receives the 25 trimmed tips, and four bolts clamp the two plates together so that each stainless-steel tube presses against the inside of a tapered tip and seals the conduit. The resulting assembly creates a compact multinozzle outlet plate from modified commercial components. Figure 4.2E shows the corresponding benchtop setup mounted on a Cartesian printing system. In this configuration, pneumatic actuation provides a simple way to test the concept, while the Cartesian machine provides a direct means of evaluating the associated deposition kinematics. Figure 4.2F shows a representative microscaffold printed with this prototype using the benchmark organic ink. The structure is deposited at 32 mm·s^{-1} under 0.69 MPa, with two passes per layer and a total of 10 layers. Figure 4.2G shows a representative close-up of the deposited pattern. Continuous parallel filaments and an identifiable periodic architecture are obtained, with an average filament diameter of $\bar{d} = 424$ µm and an average pore size of $\bar{p} =$

231 µm. Simultaneous extrusion through all 25 outlets is achieved, and visual observations do not reveal a marked position-dependent shortage across the array. The main result of this prototype lies in the combined feasibility of compact outlet packing, multichannel flow splitting, and controlled deposition. The trimmed-tip approach makes it possible to fit a dense tapered array within the footprint imposed by a larger reservoir. The printed result shows that this arrangement supports parallel filament deposition in a coherent two-dimensional pattern and that the associated kinematics remain compatible with microscaffold fabrication. The prototype therefore validates the concept as a design trial and supports the transition toward a denser and more integrated multinozzle architecture.

The assembled concept nevertheless remains limited as a printhead solution. Trimming and assembly are labor-intensive, alignment depends on manual handling, and the concept is restricted here to low-pressure operation with organic ink. The upper manifold remains reusable because its larger passages are accessible for cleaning, whereas the trimmed outlet tips can be replaced between runs. Even so, the overall architecture remains poorly suited to robust long-term integration in the high-pressure LM^2 system. The concept establishes the feasibility of the approach, but it does not provide the final printhead configuration.

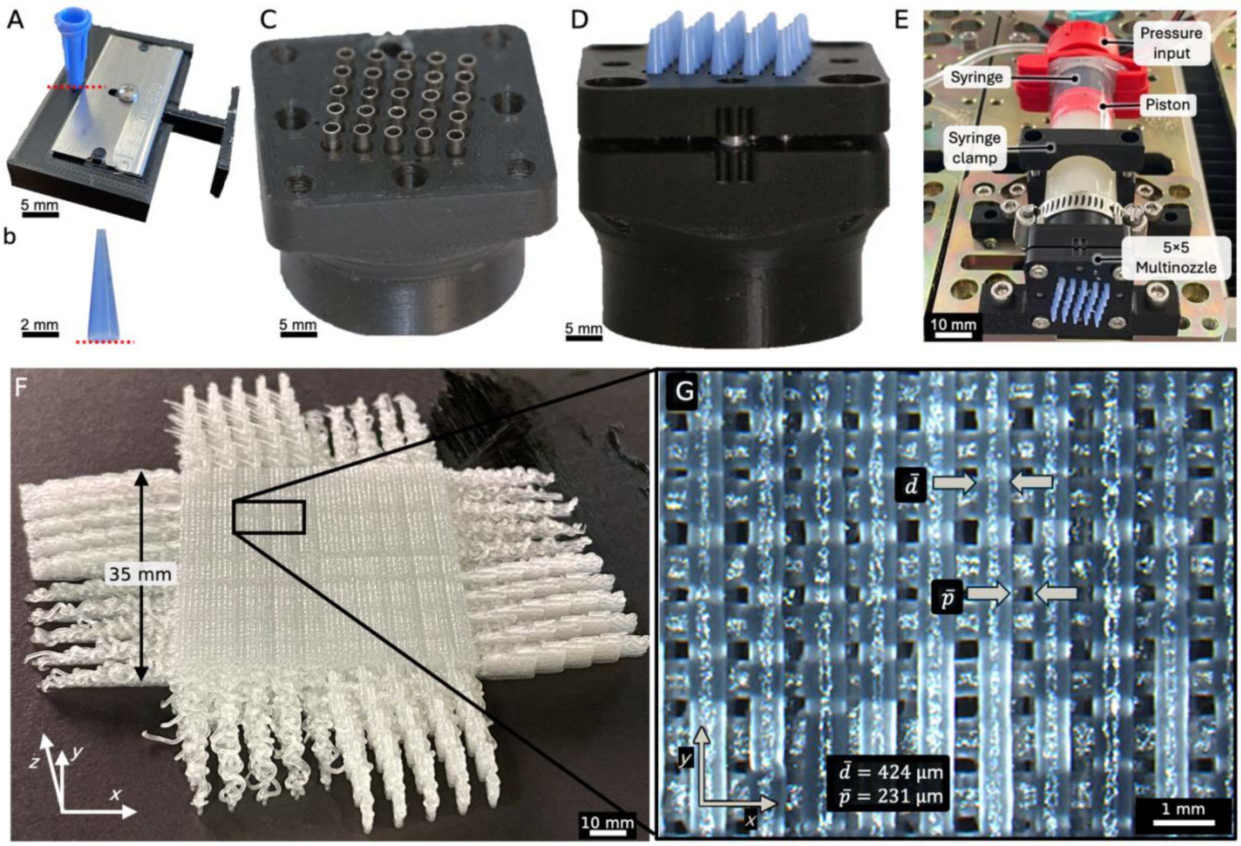

Figure 4.2: Preliminary multinozzle prototype based on commercial tapered dispensing tips. a) Custom trimming jig composed of a two-part FFF-printed body and a sliding razor-blade carriage, used to position and cut tapered tips. b) Representative trimmed commercial tapered tip. c) Compact manifold with stainless-steel tube inserts bonded into the body to provide leak-tight seats for the truncated tips. d) Assembled 5 × 5 prototype (N = 25) illustrating the packing density achievable with shortened tips. e) Benchtop extrusion setup mounted on the Aerotech system, including syringe, piston, pressure inlet, clamp, and installed multinozzle. f) Organic ink microscaffold printed with 2 passes per layer of 5 × 5 multinozzle. g) Enlarged view of the printed structure, showing an average filament diameter $\bar{d}$ = 424 µm and average pore size $\bar{p}$ = 231 µm.

4.3 Manufacturing Strategy for a Replaceable Tapered Array

The retained printhead must integrate 36 tapered channels within the footprint imposed by the reservoir while preserving fine outlet dimensions and remaining practical to replace when processing curable filled thermosetting materials. The fabrication strategy must therefore provide sufficient geometric freedom for a dense converging channel network while maintaining a simple and robust support structure.

Figure 4.3 shows the retained printhead assembly. Figure 4.3A shows the outlet region mounted at the end of the reservoir, with the SLA-fabricated multinozzle array and the titanium backing plate positioned above a microscaffold printed with the final 36-nozzle architecture. The outlet arrangement shows that each subsequent nozzle row places additional nozzles between those of the first row, increasing outlet density within the available footprint and supporting a denser deposition pattern than a single-row configuration with the same within-row pitch. Figure 4.3B shows a sectioned SLA array assembled with the backing plate. The tapered channels remain continuous through the full outlet region and are entirely formed within the printed component.

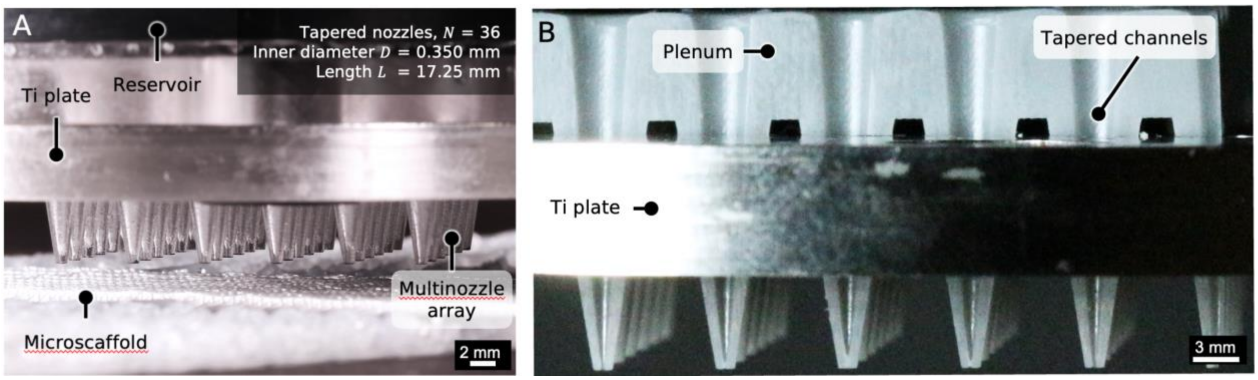

Figure 4.3: Retained printhead assembly and fabrication strategy. (a) Close-up of the final outlet region mounted at the end of the reservoir, showing the SLA-fabricated multinozzle array and the titanium backing plate above a microscaffold printed with the final 36-nozzle architecture. (b) Cross-sectional view of a sectioned SLA array assembled with the backing plate, showing the tapered channels fully defined within the printed component. The figure highlights the separation between the replaceable SLA-defined flow path and the reusable metallic structural support.

The retained architecture assigns distinct functions to these two elements. The SLA array carries the full flow-path geometry and integrates the plenum and tapered channels into a single replaceable component. The tapered nozzles themselves can withstand the pressure conditions of the LM^2 platform because their small radius limits the required wall thickness. The critical region is the plenum, where the large reservoir diameter transfers the pressure load to a broad perforated SLA section. The titanium backing plate therefore provides structural support to the plenum while remaining outside the flow path. In that sense, the printhead is conceived as semi-disposable: the SLA multinozzle array is replaced when cleaning becomes impractical, while the titanium backing plate is reused as the structural support of the assembly. The extruded material remains confined to the SLA-defined channels and does not contact the metallic reinforcement element downstream of the reservoir.

This arrangement avoids the assembly complexity of the preliminary commercial-tip concept while preserving the geometric freedom required for a dense tapered array. It also supports rapid design iteration, since nozzle diameter, channel length, and taper half-angle can be modified directly in the digital model and implemented by reprinting the SLA array. Changes to nozzle spacing require a corresponding modification of the backing plate, but this part remains simple and inexpensive to machine because it consists only of through-holes and does not contact the flow. Detailed fabrication parameters and dimensional characterization of the printed arrays are presented in Chapter 5.

4.4 Post-Extrusion Microstructural State of EC3515-10%FS

EC3515-10%FS contains hollow glass bubbles whose integrity influences both the rheology of the material during extrusion and the internal structure of the deposited composite. Figure 4.4 presents the post-extrusion microstructural state of EC3515-10%FS after curing inside the nozzle following printing.

Figure 4.4A shows representative μCT slices together with the corresponding segmentation sequence. The raw greyscale image reveals a heterogeneous microstructure with visible contrast between the continuous matrix phase, intact glass bubbles, voids, and irregular high-density fragments attributed to fractured bubble walls. The segmented views isolate intact bubbles, porosity, and their combined distribution, making visible the coexistence of preserved inclusions, collapsed bubbles, and secondary voids. Angular glass fragments embedded within the matrix are also observed and are consistent with local mechanical failure of hollow glass bubbles.

Figure 4.4B shows magnified views of the segmented phases extracted from the μCT data. Intact glass bubbles largely preserve a near-spherical morphology, whereas damaged regions are associated with irregular voids and angular debris. Quantitative analysis of the segmented volume gives approximately 20.2 vol.% intact glass bubbles, 5.8 vol.% porosity, and 74.0 vol.% of a continuous matrix phase that includes the epoxy resin together with unresolved fine fillers such as fumed silica and carbon black.

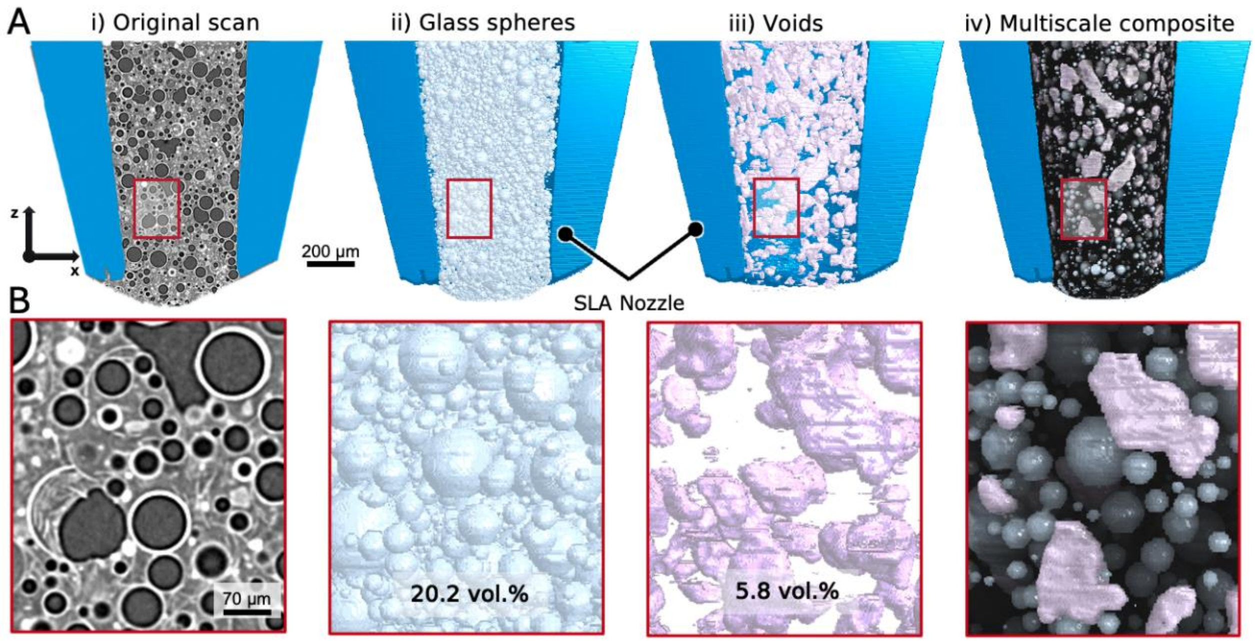

Figure 4.4: Post-extrusion microstructural state of EC3515-10%FS after curing inside the nozzle following printing. (A) Representative µCT slice and corresponding segmentation sequence showing the continuous matrix phase, intact glass bubbles, porosity, and fractured-bubble debris. (B) Magnified views of the segmented phases highlighting the morphology of preserved bubbles, irregular voids, and angular glass fragments. The figure shows that the post-extrusion material contains both intact and damaged hollow glass bubbles, indicating partial rather than uniform filler degradation.

These observations indicate that filler degradation remains partial rather than uniform in the post-extrusion material. The predominance of intact bubbles shows that the hollow filler population is not subjected to complete bulk crushing. At the same time, fractured bubbles, irregular voids, and glass fragments confirm that local microstructural damage is present after extrusion. Because some damage may already be introduced during handling or mixing, the fractured features observed here cannot be attributed exclusively to the printing step. The post-extrusion microstructure nevertheless remains consistent with localized stress concentrations within the nozzle rather than homogeneous collapse of the entire bubble population.

4.5 Supporting Digital Developments

Two supporting digital developments accompany the retained printhead architecture. One preserves a rapid first-order comparison tool for tapered channels under the pressure limit of the LM^2 platform. The other adapts the existing scaffold-generation logic to deposition strategies that differ from those used previously. Neither development defines the printhead architecture by itself, but both support its interpretation and implementation.

4.5.1 Extension of the MEPM for Tapered Nozzles

The Multinozzle Extrusion Prediction Model (MEPM), introduced in previous work for cylindrical multinozzle geometries (Chauvette, 2021), is extended in the present project to account for tapered channels. The original implementation is developed in MATLAB. In the present work, the model is rewritten in Python in order to preserve the existing logic while improving compatibility with the current digital workflow and facilitating interaction with the toolpath-generation environment.

The adapted MEPM preserves a rapid first-order comparison framework for cylindrical geometries and adds a tapered-channel formulation under the same pressure-limited conditions. An analytical expression for power-law flow in converging channels is introduced while the internal structure of the original model is retained. Appendix A summarizes the corresponding formulation, its algebraic integration into MEPM, and its principal limitations.

4.5.2 Extension of the MTG

The Multinozzle Toolpath Generator (MTG), developed in previous work for robotic microscaffold fabrication [72], is formulated around the earlier linear multinozzle architecture. For the present 6 × 6 printhead, only minor modifications are required for basic use of the generator. A new tool entry is introduced with the appropriate number of nozzles and effective filament spacing. Under these conditions, the generator remains usable.

Additional limitations appear when denser deposition strategies are considered. In its original form, the MTG is restricted to odd pass counts. That restriction does not prevent execution of the retained scaffold strategy used in the present work, but it becomes limiting when interlaced deposition is considered as an extension. Interlacing introduces a second pass offset between previously deposited filaments and therefore makes it possible to reduce effective pore size without decreasing nozzle spacing. For the present tapered array, such a strategy is relevant because the larger inlet diameters constrain the minimum achievable physical pitch. Accordingly, an even number of passes is required for interlaced deposition, which motivated the modified implementation.

The corresponding adaptation modifies the sequencing logic so that even-pass deposition remains compatible with deterministic cyclic execution. Appendix B documents both the original formulation and the modified four-layer logic. The adapted MTG therefore extends the applicability of the original generator to denser deposition patterns while preserving the geometric definition of the scaffold paths.

4.6 Chapter Summary

This chapter presented complementary technical developments associated with the final tapered multinozzle architecture reproduced in Chapter 5. These developments include a preliminary design trial based on assembled commercial tapered tips, the retained fabrication strategy combining an SLA-defined flow path with a reusable titanium backing plate, and the supporting digital developments associated with prediction and toolpath generation.

CHAPTER 5 ARTICLE 1: ADDITIVELY MANUFACTURED TAPERED MULTINOZZLE ARCHITECTURE FOR HIGH-FLOW DIRECT INK WRITING OF HIGHLY VISCOUS THERMOSET COMPOSITES

Raphaël Plante, Ruby Rozier, Rouhollah D. Farahani, Sampada Bodkhe and Daniel Therriault*

Laboratory for Multiscale Mechanics (LM2), Department of Mechanical Engineering, Polytechnique Montréal, Montréal, Canada

Submitted to Additive Manufacturing on March 16, 2026

Abstract

Direct ink writing (DIW) of highly viscous thermoset composites is constrained by the pressure required to extrude fine filaments at high speed. This work presents a low-cost multinozzle alternative: a 36-outlet (6 × 6) tapered polymer array fabricated by consumer-grade stereolithography and supported by a reusable backing structure that carries the mechanical load independently of the flow path. This design makes dense multinozzle printing more accessible, easier to iterate, and more practical for reactive and particle-filled thermoset materials. Characterization across 12 arrays and 432 nozzles confirmed dimensional viability, with measured outlet diameters of 255.7 ± 14.1 µm for the 230 µm design and 370.0 ± 22.5 µm for the 350 µm design, and low internal channel roughness (Ra = 0.50 ± 0.21 µm). Compared with the cylindrical reference multinozzle, the tapered design reduced the pressure required at 200 mm/s by 71.6% for a wax-based reference ink and by 84.6% for a silica-filled thermoset ink. For a highly viscous glass-microsphere-filled thermoset composite ink, scaffold fabrication was achieved at 100 mm/s under approximately 11 MPa using 350 µm outlets with total flow rate exceeding 500 mm^3/s, conditions under which comparable cylindrical configurations were not operable. An 18-layer scaffold was completed in under 3.5 min, with 85.6% of surface points within ±100 µm of the target geometry. Overall, the 36-nozzle architecture reduces the estimated fabrication time of a representative planar structure from 40.8 h with a single nozzle to 1.1 h at the same deposition speed.

Keywords: Direct ink writing; multinozzle printhead; high throughput printing; highly viscous thermosets

5.1 Introduction

Direct ink writing (DIW) is an extrusion-based three-dimensional (3D) printing process that enables the fabrication of architected materials across applications including biomedical scaffolds [73], multifunctional lattices [3], and structural composites [15]. DIW relies on extrudable materials, referred to as inks, that must flow when subjected to shear stresses within the nozzle and must, upon deposition, rapidly recover sufficient stiffness to support their own weight and subsequent layers [15]. In structural and multifunctional applications, DIW increasingly targets composite formulations [3], [20], which offer application-specific properties but often exhibit elevated apparent viscosities within the shear-rate range relevant to extrusion [31]. Because the volumetric flow rate required to sustain a given printing speed depends on material rheology and nozzle geometry, increasing deposition speed or reducing outlet diameter requires a higher extrusion pressure. Under practical system pressure limits, this coupling constrains the attainable combination of throughput and filament diameter. This constraint becomes particularly restrictive in applications such as aerospace abradable coatings [8] and acoustically functional surfaces, where sub-millimeter features must be deposited over surfaces spanning tens of centimeters [4],[74], [75].

Conventional DIW platforms typically address viscous inks by increasing nozzle diameter to reduce hydraulic resistance or by slowing the printing speed when fine features are needed. Both approaches fundamentally limit scalability: larger diameters degrade resolution, while slower deposition rates yield impractically long build times for mesoscale and large-area structures. Multinozzle printheads introduce an additional degree of freedom in the pressure–throughput relationship by parallelizing extrusion across multiple outlets, thereby increasing deposition rate without increasing the flow rate per nozzle or pressure demand. Prior works have demonstrated multinozzle arrays for high-throughput microvascular printing [55], adaptive multi-material deposition [56], modular arrays from commercial nozzles [76] and rapid fabrication of microscaffold networks [54]. Most existing multinozzle architectures employ constant-diameter (cylindrical) channels, in which the flow remains confined to the minimum cross-section along the full channel length. This configuration limits operation at fine diameters for viscous materials, even in high-pressure systems [60].

Converging or tapered nozzles have been shown through analytical and numerical studies to reduce viscous dissipation and redistribute shear stresses relative to cylindrical channels of equal outlet diameter [41], [77]. By shortening the fraction of the flow path confined to the minimum cross-section, tapered geometries can significantly reduce pressure drop while preserving outlet resolution. This behavior is particularly advantageous for materials containing fragile fillers such as hollow microspheres, where excessive stresses can cause particle fracture or undesirable microstructural changes [78]. Despite these advantages, tapered geometries have so far been applied primarily to single-nozzle dispensing systems, and their integration into dense multinozzle architectures suitable for high-throughput DIW remains limited.

Existing multinozzle DIW printheads are commonly fabricated through subtractive machining [55] or meticulously assembled from multiple components [56]. These approaches although typically intended for reuse, become difficult to clean when processing thermosetting composite inks, where residual material can cure within the multichannel hardware. In addition, the fabrication of non-cylindrical internal geometries such as tapered channels is challenging using conventional methods, which has limited their implementation in dense multinozzle arrays.

Recent advances in additive manufacturing (AM) have enabled the fabrication of customized DIW nozzles with intricate internal geometries tailored to specific applications [51], [68], [69], [58]. In particular, stereolithography (SLA) has been used to realize complex channel architectures, including multicore and coaxial printheads with tapered internal geometries [69] and integrated fluid channels that would be difficult to produce using subtractive techniques. Such approaches demonstrate the feasibility of fabricating reproducible nozzles with controlled internal channel profiles and fine outlet dimensions directly from digital designs. These developments expand the design space of DIW printheads by permitting internal geometries and dense channel networks that were previously constrained by manufacturing limitations.

In this work, a low-cost tapered multinozzle architecture intended for semi-disposable use is presented for DIW of highly viscous thermosetting composites. The proposed design uses nozzle tapering and dense parallelization to modify the pressure–throughput relationship while preserving the outlet diameter. The main objectives of this study are: (1) to develop a multinozzle architecture that reduces pressure demand relative to cylindrical configurations under identical constraints, and (2) to demonstrate its usability across multiple inks representative of distinct viscosity regimes through quantitative pressure–speed characterization and geometric fidelity assessment.

5.2 Methods and Materials

5.2.1 Overview of the DIW Platform

Figure 5.1 shows the direct ink writing (DIW) platform used in this work, the tapered multinozzle printhead, the associated deposition kinematics, and the representative scaffold geometry used for evaluation. Figure 5.1A presents the experimental platform, where motion is handled by a six-axis industrial robot (FANUC M-20iD/25, FANUC Corp., Japan) equipped with a custom piston-driven hydraulic extrusion unit capable of inlet pressures up to 20 MPa (Mëkanic – FACMO Chair collaboration, Montreal, Canada). Material was loaded into a 250 cm^3 cylindrical reservoir and extruded by the axial displacement of a 50.8 mm diameter piston. Piston position was monitored using a linear encoder (Temposonics R-Series RH, MTS Systems Corp., NC, USA), enabling velocity-controlled extrusion in which volumetric flow rate was imposed through piston motion rather than direct pressure regulation.

Figure 5.1B shows the tapered multinozzle printhead investigated in this work. The printhead consists of a polymer array integrating tapered channels within a single component and was developed to operate within the pressure limits of the platform while enabling parallel extrusion at controlled outlet diameter. Figure 5.1C illustrates the corresponding deposition kinematics, in which multiple outlets deposit parallel filaments simultaneously in a single pass.

Figure 5.1D shows the representative orthogonal microscaffold geometry used for evaluation, with a nominal filament diameter of 350 µm, an in-plane spacing of 1 mm, and a total height of 5.6 mm. Because the inlet diameter of each tapered channel exceeds its outlet diameter, the minimum achievable nozzle pitch is constrained by internal channel geometry rather than outlet spacing alone. Figure 5.1 therefore defines the main architectural constraint addressed in this work: achieving compact multinozzle integration while maintaining low hydraulic resistance and controlled filament spacing.

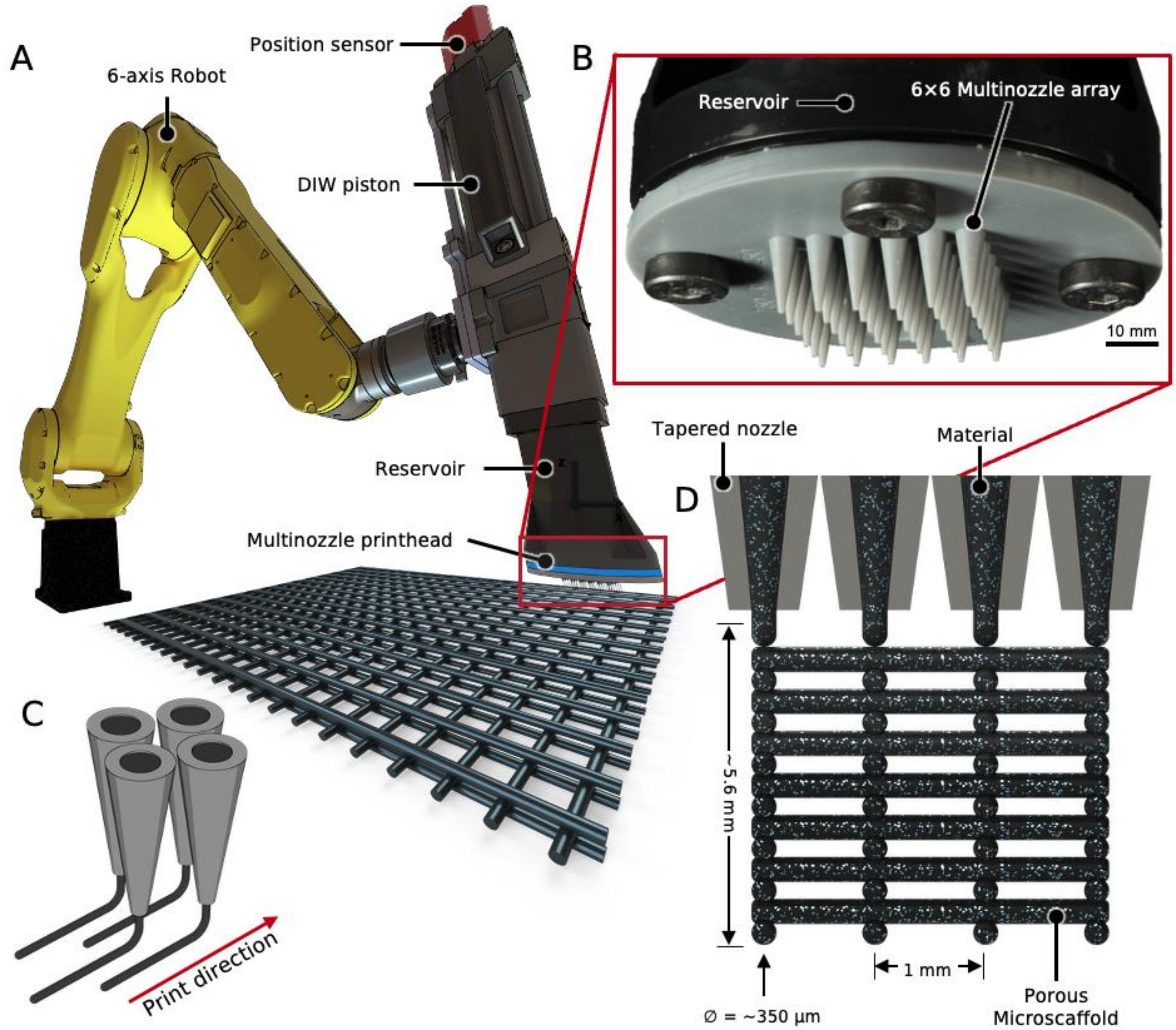

Figure 5.1: (A) DIW platform comprising a six-axis robotic arm and a custom piston-driven hydraulic extrusion unit capable of pressures up to 20 MPa; the perspective view is adjusted for clarity and is not to scale. (B) Tapered multinozzle printhead integrating the nozzles within a single polymer component. (C) Schematic of a 2×2 grid multinozzle deposition kinematics showing simultaneous extrusion of parallel filaments along the printing direction. (D) Representative orthogonal porous microscaffold geometry used to evaluate the performance of the present multinozzle design, with a nominal filament diameter of 350 μm, in-plane spacing of 1 mm, and desired stacking height of 5.6 mm.

5.2.2 Materials

Three representative ink systems were selected to validate the proposed tapered multinozzle architecture across a wide range of apparent viscosities and microstructural complexity. Materials were chosen from low-viscosity model inks to industrial-grade, particle-filled thermosetting composites.

A wax-based organic ink was used as shear-thinning reference material. The ink consisted of 60 wt.% petroleum jelly (Vaseline, Unilever, Canada) and 40 wt.% microcrystalline wax (SP-18, Strahl & Pitsch, USA), following established formulations and preparation reported in the literature [79], [10]. This material represents the lowest-viscosity system investigated and was used to assess extrusion behavior and flow uniformity across the multinozzle array in the absence of curing effects.

An epoxy-based thermosetting ink was prepared from EPON 828 resin (Hexion) and EPIKURE 3274 hardener at a 10:4 mass ratio. To impart yield stress and shear-thinning behavior suitable for DIW, the formulation was filled with 14 wt.% hydrophilic fumed silica (CAB-O-SIL TS-720, Cabot), following the formulation and preparation strategy established by Chauvette et al. [17]. This system represents an intermediate-viscosity thermoset with time-dependent curing behavior, providing a practical benchmark between non-curing model inks and highly filled industrial composites.

An aerospace-grade abradable epoxy composite (EC-3515 B/A, 3M), consisting of a two-part epoxy matrix prefilled with hollow glass microspheres, was used as the primary industrial validation material. As received, this material exhibits very high apparent viscosity and insufficient shape retention for DIW. To enable stable filament shape retention, a fixed addition of 10 wt.% hydrophobic fumed silica was incorporated into the mixed A/B system (mass ratio 94:100), using a low-speed mechanical mixer (KSM35, Kitchen in the box) at the lowest setting until uniform dispersion was achieved. The total time between initial mixing and printing was approximately 40–50 min.

All materials were extruded at ambient temperature in an uncured state using the same hydraulic extrusion system.

5.2.3 Printing protocol and toolpath execution

Microscaffolds were fabricated as periodic orthogonal filament lattices. Each layer consisted of parallel filaments deposited at constant linear speed, with a nominal center-to-center spacing of 1 mm. For a filament diameter of 350 µm, this corresponds to a pore size on the order of 650 µm. Upon completion of a layer, the printhead was translated vertically by a layer height equal to 80% of the nozzle diameter. Successive layers were deposited along the orthogonal direction without rotation of the printhead. Continuous extrusion was maintained throughout deposition; no active flow interruption was applied between filaments or layers. During interlayer repositioning, the toolpath was cleared slightly outside the printed surface to avoid filament interference. Toolpaths were generated using a modified version of the Multinozzle Toolpath Generator (MTG) [54], in which the geometric parameters of the present printhead (outlet diameter, nozzle count, and nozzle pitch) were incorporated. The resulting toolpaths were converted to a FANUC-compatible program using RoboDK (RoboDK Inc., Canada). The multinozzle printhead and substrate reference frame were calibrated using a three-point method prior to printing. Extrusion rate was held constant during each experiment. An empirical extrusion correction factor of up to 1.2 was applied when necessary.

5.2.4 Characterization

Characterization was performed at three levels: (i) dimensional and surface characterization of the SLA-fabricated multinozzle arrays, (ii) optical and electron microscopy of printed filaments and scaffolds, and (iii) scaffold-scale geometric fidelity assessment by X-ray microcomputed tomography (μCT).

5.2.4.1 Multinozzle dimensional and surface characterization

Dimensional accuracy of the SLA-fabricated multinozzle arrays was evaluated using digital optical microscopy (VHX-7000, Keyence Corporation, Canada). Dimensional measurements were obtained with the integrated XY metrology module (VHX-H3M3). Outlet geometry was quantified by automated brightness-threshold segmentation of the outlet openings in underside images of the arrays. For each array, the projected area of all 36 outlets was measured and converted to an equivalent circular diameter. This analysis was performed for two nominal outlet geometries investigated in this work, namely 350 μm arrays (n = 12 arrays, 432 nozzles total) and 230 μm arrays (n = 3 arrays, 108 nozzles total). Arrays fabricated individually and, when applicable, in vertically stacked builds were analyzed using the same procedure.

Internal surface roughness of representative tapered channels was evaluated after longitudinal sectioning of the printed arrays. Roughness measurements were performed using the 3D line roughness module (VHX-H5M, Keyence Corporation, Canada). Profiles were acquired along the axial flow direction, and roughness parameters were computed according to ISO 4287 definitions using a cutoff wavelength of λ_c= 0.25 mm and an evaluation length of at least 1.25 mm. Multiple traces were acquired for each measurement location and reported as mean ± standard deviation.

5.2.4.2 Optical microscopy of printed structures

Printed filaments and microscaffolds were examined using digital optical microscopy (VHX-7000, Keyence Corporation, Canada) to assess filament continuity, pore morphology, and overall scaffold regularity. Filament-width measurements were obtained from optical micrographs using the integrated XY metrology module (VHX-H3M3) and are reported as mean ± standard deviation. For the EC3515-10%FS scaffolds, additional side-view observations were obtained from razor-sectioned samples to examine layer stacking, local compaction near the substrate, and cross-sectional scaffold morphology.

5.2.4.3 Scanning Electron Microscopy (SEM)

Nozzle-tip morphology and the surface morphology of extruded filaments and printed scaffolds were examined using a tabletop scanning electron microscope (TM3030 Plus, Hitachi, Japan). Samples were mounted on aluminum stubs using conductive carbon tape and imaged without conductive coating. Observations were performed in low-vacuum mode at an accelerating voltage of 15 kV with a working distance of approximately 7–8 mm. Images were acquired using the instrument's mixed signal detector (secondary and backscattered electron signals) over magnifications typically ranging from 50× to 2000×. SEM observations were used qualitatively to assess outlet circularity, surface texture associated with the layer-wise SLA fabrication process, and microscale surface features of the extruded thermoset composite filaments.

5.2.4.4 X-ray microcomputed tomography

Selected specimens were characterized by X-ray microcomputed tomography (Xradia 520 Versa, Zeiss, Canada). For scaffold-scale geometric fidelity analysis, printed microscaffolds were scanned at 50 kV and 4 W using 2400 projections, with a voxel size of 12 μm for mesoscale analysis. Higher-resolution scans were also performed on selected local features at a voxel size of 1.50 μm.

Reconstruction and segmentation of volumes was conducted in Dragonfly (Comet Technologies, Canada) using a pretrained U-Net (dl-5 ifc-64 slice-3) model that was fine-tuned on user-labeled slices to accurately classify material phases. For the microscaffold, a triangular surface mesh was extracted from the segmented solid phase and registered to the corresponding CAD geometry in CloudCompare (version 2.14.0) using the Align tool. The CAD geometry was retained as the reference entity, while the μCT-derived mesh was treated as the aligned entity. Registration was performed from manually selected corresponding points with scale fixed at 1.0, so that only rigid translation and rotation were applied. The root mean square residual error (RMS) was 0.0745 mm, computed on 50,000 points with theoretical overlap of 100%. Cloud-to-mesh (C2M) signed distances were computed and visualized to quantify deviations and evaluate geometric fidelity.

5.2.5 Fluid Modeling

Flow through the nozzle was simulated using COMSOL Multiphysics 6.3 in a 2D axisymmetric formulation. The steady-state, laminar, incompressible Navier–Stokes equations were solved using quadratic velocity and linear pressure elements (P2–P1). The fluid was modeled as a generalized Newtonian power-law material with consistency index $K = 3280$ Pa s^n and flow behavior index $n = 0.49$, corresponding to shear-thinning behavior. No-slip boundary conditions were imposed along the channel walls, and axisymmetry was enforced along the centerline. A fully developed flow condition was prescribed at the inlet via a volumetric flow rate corresponding to the target exit velocity, and an atmospheric pressure boundary condition was applied at the outlet. The nonlinear system was solved using a direct solver (PARDISO). The domain was discretized using a free triangular mesh calibrated for fluid dynamics, comprising 14,672 elements (13,632 triangles and 1,040 quadrilaterals). Global mesh sizing included a maximum element size of 0.0527 mm, minimum element size of 0.00234 mm, and a growth rate of 1.15. Local refinement was applied near the outlet region, with a minimum element size of 4.68×10^{-4} mm.

5.3 Tapered Multinozzle Architecture: Design, Fabrication, and Characterization

5.3.1 Existing Multinozzle Architectures and Practical Design Constraints

Parallelization, defined as the simultaneous deposition of multiple filaments from separate nozzles during a single toolpath pass, has been proposed to increase deposition rate in DIW systems. Several multichannel configurations have been reported, differing in nozzle count, layout, geometric profile, and fabrication approach. Representative multinozzle and reference dispensing architectures from the literature are summarized in Table 5.1 to contextualize the design space addressed in this work.

Table 5.1: Geometric and fabrication characteristics of representative DIW nozzle architectures

Nozzle Count	Layout	Nozzle Profile	Outlet Diameter (mm)	Length (mm)	Aspect ratio	Fabrication approach	Ref
1	-	Cylindrical	0.10-1.57	6.35 (short) 38.1 (long)	-	Injection molded polymer + metal tube insert	Nordson cylindrical tips [80]
1	-	Tapered	0.20-1.60	17.25	-	Injection molded polymer	Nordson SmoothFlow tapered tips [41]
5	Linear	Cylindrical (bent)	1.0	38	38	Connector-based assembly	Al-Ali et al. [76] (2025)
16	Linear	Cylindrical	1.37	50	36.5	FFF manifold + assembled metal tube nozzles	Uzel et al. [56] (2022)
26	Linear	Cylindrical	0.25	6.5	26	Micromachined metallic, direct-feed manifold	Chauvette et al. [54] (2021)
32	Array	Cylindrical	0.61	40	65.6	FFF branched manifold + connector based assembly	Weiss et al. [59] (2025)
64	Linear	Cylindrical	0.2	2.3	11.5	Micromachined acrylic branched manifold	Hansen et al. [55] (2013)

Table 5.1 compiles the principal geometric characteristics of these systems, including nozzle count, layout, internal channel profile, outlet diameter, channel length, and fabrication approach. This dataset is subsequently used in Section 5.3.6 to evaluate how different nozzle geometries influence predicted throughput under identical pressure constraints, enabling direct performance comparison between existing cylindrical architectures and the multinozzle design proposed in this work. The architectures summarized in Table 1 reflect different design motivations and fabrication strategies. Several systems rely on connector-based assemblies in which a manifold distributes material to interchangeable dispensing tips or tubing segments. Such configurations emphasize modularity and allow nozzle diameter or length to be selected using commercially available

components, similar to conventional DIW systems that employ replaceable dispensing tips. These architectures can also facilitate multimaterial deposition when multiple material inputs are used. In contrast, other implementations rely on integrated manifolds in which the channel network is formed directly within the manifold body through machining, additive manufacturing, or microfabrication, sometimes complemented by bonded covers or inserted outlet tubes. Such systems are generally intended for repeated use and primarily target increased deposition rate through extrusion parallelization.

When processing reactive, particle-filled, or high-viscosity formulations, integrated multichannel assemblies can introduce additional operational constraints. Residual material must typically be removed by flushing, mechanical clearing, or partial disassembly. As channel diameter decreases and nozzle density increases, the sensitivity of these systems to incomplete cleaning also increases [10], [71]. Although such considerations are rarely emphasized in the literature, they can become significant in both research and industrial environments where material changeover and contamination control are required. These operational constraints highlight the potential value of multinozzle architectures that remain economically replaceable while maintaining high outlet density and controlled filament dimensions. Geometrically, most reported multinozzle systems employ cylindrical channels. Reported outlet diameters range from 0.20 to 1.37 mm, while channel aspect ratios vary widely depending on the application. Consequently, increases in volumetric deposition rate are generally achieved by increasing the number of outlets or by raising the available extrusion pressure rather than by modifying channel geometry to reduce hydraulic resistance.

Accordingly, the design of a multinozzle architecture for pressure-limited DIW must consider not only extrusion parallelization and packing density, but also channel-scale hydraulic efficiency and practical replaceability. The limited availability of economically replaceable multichannel architectures within the existing landscape motivates the exploration of alternative fabrication strategies that reconcile throughput scaling with operational robustness.

5.3.2 Grid-Based Parallelization Strategy for Scaffold Fabrication

The retained multinozzle layout must satisfy two coupled requirements: fitting the largest possible number of nozzles within the available printhead footprint and generating the filament spacing required for scaffold fabrication. In parallel deposition, the center-to-center nozzle pitch p influences the center-to-center filament spacing s. For cylindrical nozzles, the inlet and outlet diameters are identical, so pitch can be reduced together with outlet diameter. For tapered nozzles, the inlet diameter is larger than the outlet diameter. Increasing taper angle or nozzle length therefore increases the inlet diameter and imposes a minimum manufacturable pitch between adjacent channels. The resulting minimum pitch constraint limits how closely tapered nozzles can be packed when deposited filament spacing remains directly tied to physical pitch.

A grid-based architecture is retained to address the packing limitation. Because the available printhead footprint is circular, a two-dimensional outlet distribution uses the available area more efficiently than a single-row arrangement while preserving a regular scaffold pattern. Figure 5.2A shows the retained grid strategy for three representative square arrays, illustrated from a bottom view of the multinozzle outlets to show the simultaneously deposited filaments. Figure 5.2A(i) presents the $N = 4$ configuration and illustrates how two orthogonal deposition passes generate the scaffold pattern in the central region. The nozzle pitch p, the resulting filament spacing s, the print directions, and the array orientation angle θ are indicated explicitly. Figure 5.2A(ii) and Figure 5.2A(iii) show the corresponding $N = 16$ and $N = 36$ configurations. In all three cases, the physical pitch p remains fixed, while the orientation angle θ decreases as nozzle count increases. The accompanying values show that increasing nozzle count reduces the effective filament spacing s while the physical pitch p remains unchanged.

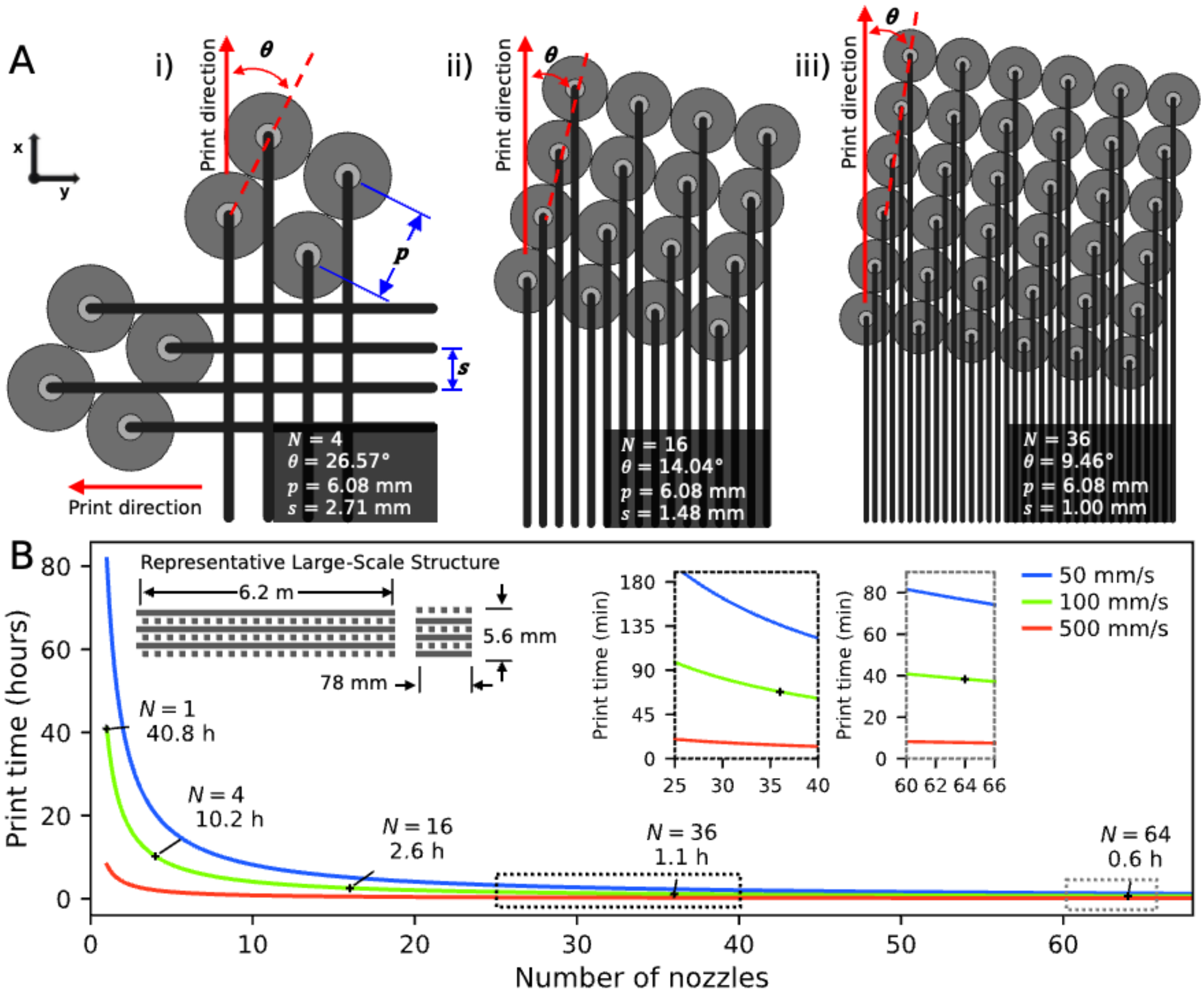

Figure 5.2: Grid-based parallelization strategy and build-rate scaling. (A) Retained multinozzle layout and filament-spacing geometry for three representative square grids: (i) $N = 4$, (ii) $N = 16$, and (iii) $N = 36$. (B) Estimated fabrication time for a representative planar structure (6.2 m × 78 mm × 5.6 mm) as a function of nozzle count at deposition speeds between 50 and 500 mm s^{-1}. Insets highlight the reduced influence of deposition speed at high nozzle count.

For the square grids considered here, the angle required to obtain equal filament spacing in the two orthogonal scaffold directions is

$$\theta = \arctan\left(\frac{1}{\sqrt{N}}\right), \tag{5.2}$$

and the effective filament spacing is

$$s = p \sin\theta \qquad (5.3)$$

Figure 5.2A explains the practical consequence of these relations. Increasing nozzle count does not change the manufacturable pitch p, which remains constrained by the inlet diameter of the tapered channels. Instead, it decreases the orientation angle θ, which in turn reduces the deposited filament spacing s. The retained grid strategy therefore provides a practical means of increasing deposition density while preserving a manufacturable tapered geometry.

Figure 5.2B shows the corresponding effect of nozzle-count scaling on fabrication time for a representative planar structure measuring 6.2 m in length, 78 mm in width, and 5.6 mm in height. The plot indicates that fabrication time decreases strongly with increasing nozzle count over the full speed range considered. At 100 mm s^{-1}, for example, the estimated build time decreases from 40.8 h for a single nozzle to 1.1 h for a 36-nozzle configuration. Increasing deposition speed also reduces fabrication time, but higher speed increases sensitivity to machine-dynamic limitations such as acceleration artefacts, vibration, and power demand. The two inset zooms show that, beyond a certain level of parallelization, the influence of printing speed becomes secondary compared with the influence of nozzle count. Around the 36-nozzle configuration, the estimated fabrication time remains below 135 min for all three deposition speeds considered, while at 64 nozzles it remains below 80 min across the same speed range. Figure 5.2B therefore shows that nozzle parallelization becomes the dominant lever for reducing fabrication time once dense arrays are reached, while further increases in deposition speed provide a smaller practical benefit.

5.3.3 Channel Geometry and Hydraulic Design

Following layout optimization, channel geometry was examined to reduce hydraulic resistance while preserving outlet diameter and array compactness. In the present work, hydraulic resistance R_h is defined as:

$$R_h = \frac{\Delta P}{Q} \qquad (5.4)$$

where$\Delta P$is the pressure drop across the nozzle and Q is the volumetric flow rate. Reducing R_h enables higher deposition speeds under a fixed pressure ceiling.

For laminar flow in a cylindrical channel, classical viscous-flow theory indicates that pressure drop scales as

$$\Delta P \propto \frac{\mu L Q}{D_{out}^4}, \tag{5.5}$$

where μ is the viscosity, L is the channel length, and D_{out} is the outlet diameter [81]. This relation highlights the linear dependence of pressure drop on channel length and the stronger sensitivity to outlet diameter. Reducing channel length therefore decreases hydraulic resistance, while decreasing outlet diameter dramatically increases hydraulic resistance.

To evaluate how channel geometry influences hydraulic resistance, finite-element simulations were performed comparing cylindrical and tapered channels with identical outlet diameters and channel lengths. The simulations were used to quantify the hydraulic advantage of tapered channels over cylindrical ones and to determine an appropriate taper angle for the multinozzle architecture. Figure 5.3 summarizes three complementary analyses used to guide channel design: pressure–velocity scaling with outlet diameter (Figure 5.3A), influence of taper angle (Figure 5.3B), and internal shear-rate distributions (Figure 5.3C).

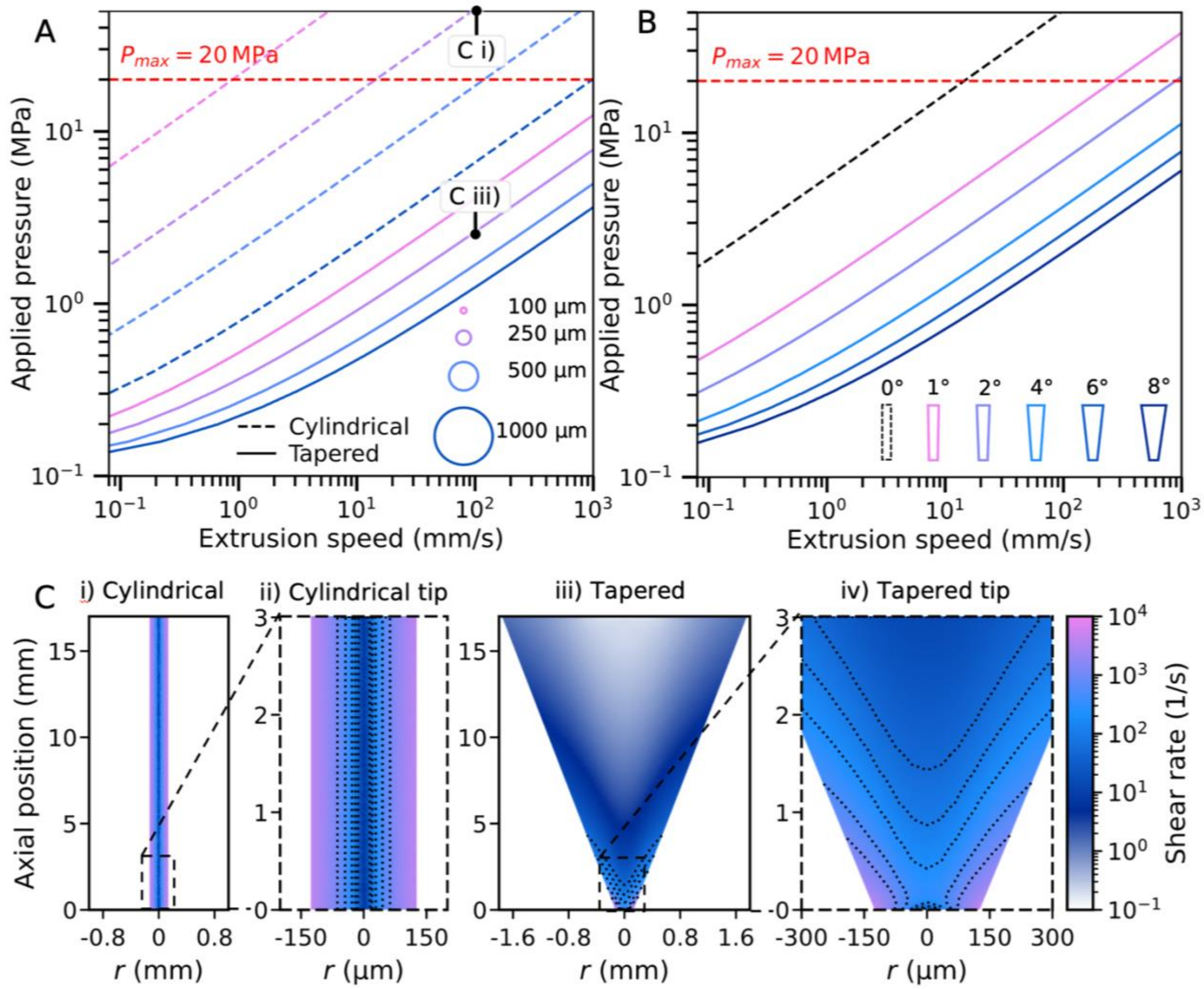

Figure 5.3: Finite-element prediction of flow behavior in cylindrical and tapered nozzle geometries.(A) Predicted extrusion pressure as a function of outlet velocity for cylindrical and tapered channels with outlet diameters ranging from 100 to 1000 µm and identical channel length (L = 17 mm). The red dashed horizontal line indicates the maximum available extrusion pressure of the system (20 MPa). (B) Predicted pressure–velocity relationships for taper half-angles ranging from 0° (cylindrical) to 8° for a fixed outlet diameter of 250 µm. (C) Simulated shear-rate distributions for cylindrical and 6° tapered channels (250 µm outlet diameter, L = 17 mm) at an outlet velocity of 100 mm s^{-1}. Full-channel views and outlet-region enlargements show that tapering confines the highest shear rates to a short region near the outlet, whereas elevated shear persists along most of the cylindrical channel.

Figure 5.3A compares the predicted extrusion pressure as a function of outlet velocity for cylindrical and tapered channels with outlet diameters of 100, 250, 500, and 1000 µm. The red dashed horizontal line indicates the maximum pressure available in the extrusion system (20 MPa). For all diameters considered, tapered geometries require substantially lower pressure to sustain a given flow rate. For example, at an outlet diameter of 250 µm and an extrusion velocity of 100 mm s^{-1}, the cylindrical channel requires approximately 51 MPa, exceeding the available pressure, whereas the tapered channel with a half-angle of 6° requires only about 2.6 MPa. This represents a reduction of more than 95% in the required pressure, demonstrating the strong hydraulic advantage of tapered geometries.

While tapering clearly reduces hydraulic resistance, the influence of taper angle must also be considered. Figure 5.3B shows the predicted pressure–velocity relationship for taper half-angles ranging from 0° (cylindrical) to 8°, for a fixed outlet diameter of 250 μm and channel length of 17 mm. Increasing the taper angle progressively reduces the pressure required to maintain a given flow rate. However, the magnitude of improvement decreases as the angle becomes larger. Increasing the half-angle from 0° to 4° reduces the predicted pressure by approximately 93%, whereas increasing it from 4° to 6° yields a smaller additional reduction of about 30%. Further increases provide diminishing returns.

Figure 5.3C shows simulated shear-rate distributions for cylindrical and 6° tapered channels with identical outlet diameter (250 μm) and length (17 mm) at an outlet velocity of 100 mm s^{-1}. Panels (i–ii) correspond to the cylindrical channel, while panels (iii–iv) show the tapered geometry, with both full-channel views and outlet-region enlargements.

In the cylindrical channel, elevated shear rates persist along nearly the entire channel length due to the constant minimum diameter. In contrast, the tapered channel exhibits substantially lower shear rates throughout most of the channel, with high shear confined primarily to a short region near the outlet. Iso-shear contours (50–10^3 s^{-1}) highlight this difference: in the cylindrical channel they extend almost uniformly along the flow path, whereas in the tapered channel they concentrate near the tip of the converging section.

Although peak wall shear rates exceed 10^3 s^{-1} in both geometries, the region subjected to these values represents only a small fraction of the channel length in the tapered nozzle. This redistribution of deformation along the converging channel accompanies the reduction in hydraulic resistance observed in Figure 5.3A and 5.3B.

5.3.4 Final Nozzle Geometry Selection

The final nozzle geometry was determined by balancing hydraulic performance with the geometric packing constraints imposed by the multinozzle layout. As shown in Figure 5.3B, increasing the taper half-angle α significantly reduces the pressure required to sustain a given flow rate. However, the magnitude of this improvement decreases as the angle increases, indicating diminishing hydraulic benefit at larger taper angles. This behavior is consistent with converging-flow studies showing that pressure losses become less sensitive to further increases in contraction angle as the flow transitions from being mainly shear-dominated to a stronger combination of shear and extensional deformation [82].

Increasing α simultaneously enlarges the inlet diameter of the channel according to

$$D_{in} = D_{out} + 2L\tan\,\alpha. \quad (6)$$

where L is the channel length and D_{out} is the outlet diameter. Because the inlet diameter determines the minimum achievable nozzle pitch within the grid layout described in Section 5.3.2, larger taper angles reduce the packing density that can be achieved within a fixed footprint. Channel length also influences this relationship. For a fixed taper angle, reducing L decreases the inlet diameter and proportionally reduces hydraulic resistance. In practice, however, the channel length must provide sufficient axial protrusion of the nozzle outlets relative to the manifold body to prevent interference with previously deposited material during printing. A clearance margin of approximately 5 mm was therefore maintained between the manifold body and the deposition plane. To satisfy this clearance requirement while maintaining structural integrity of the array, the channel length was fixed at 17.25 mm. For this length, increasing the taper half-angle from 4° to 8° increases the inlet diameter from approximately 2.73 mm to 5.13 mm, introducing a trade-off between hydraulic efficiency and array compactness. Considering these constraints, a half-angle of 5.3° was selected as a practical compromise between hydraulic performance and geometric packing. For this geometry the inlet diameter is approximately 3.5 mm, which remains compatible with the 50.8 mm footprint while allowing a minimum nozzle pitch of approximately 6.08 mm and preserving sufficient material between adjacent channels for structural integrity. At this angle, the pressure required to sustain a given outlet velocity remains more than 90% lower than for an equivalent cylindrical channel, while maintaining compatibility with the multinozzle layout. Based on these constraints, the final architecture consists of a 6 × 6 tapered multinozzle grid comprising 36 nozzles, each with a half-angle of 5.3° and a length of 17.25 mm. With a nozzle pitch of approximately 6 mm, the selected grid orientation produces an effective filament spacing of approximately 1 mm, as defined by the geometric relationship introduced in Section 5.3.2.

5.3.5 Printhead Fabrication and Dimensional Characterization

The multinozzle arrays were fabricated using stereolithography (SLA) to produce the tapered microchannel geometry identified in the preceding design analysis. Each array was printed as a single monolithic component containing the 36 tapered channels using a commercial SLA printer (Formlabs Form 4, Formlabs Inc., USA) with a rigid photopolymer resin (Grey V5). Preliminary mechanical sizing indicated that the printed array alone would require an impractically thick reservoir-side manifold region to sustain operation at pressures up to 20 MPa. The array was therefore mechanically supported by a machined titanium backing plate located outside the flow path. This plate carries the majority of the structural load while the SLA-fabricated array provides the fluid channels, enabling the multinozzle component to function as a low-cost disposable element. Dimensional characterization of the nozzle outlets was performed using optical microscopy as described in Section 5.2.4.1. Figure 5.4A shows a top view of a representative 6 × 6 array together with a magnified view of a single row, illustrating the small outlet size and the overall uniformity of the apertures. Figure 5.4B presents the measured outlet diameter distributions for both nominal 230 µm and 350 µm nozzle geometries. For individually fabricated arrays, the outlet diameter distributions remained centered near the nominal design values. For the 350 µm geometry, vertically stacked fabrication of multiple arrays was also evaluated to increase production throughput. In these stacked builds, arrays located in lower positions exhibited a shifted outlet diameter distribution centered near approximately 380 µm, whereas the topmost array remained comparable to individually fabricated arrays. Surface morphology of the nozzle outlets was examined using scanning electron microscopy (Section 5.2.4.4). Figure 5.4C shows a representative nozzle tip at high magnification. The outlet aperture exhibits good circularity with minor surface texture associated with the layer-wise SLA fabrication process, which did not produce observable flow instabilities during extrusion. Internal channel surface quality was evaluated by sectioning representative nozzles and measuring roughness profiles along the axial flow direction as described in Section 5.2.4.1. Figure 5.4D shows a cross-section of a tapered channel together with a representative roughness measurement region. The measured roughness was R_a = 0.50 ± 0.21 µm, which remains small relative to the nozzle diameter and is therefore not expected to significantly influence the hydraulic behaviour of the channels.

Together, these observations confirm that SLA fabrication provides sufficient dimensional accuracy and surface quality to implement the tapered multinozzle geometry while maintaining the rapid and low-cost fabrication required for disposable printhead components.

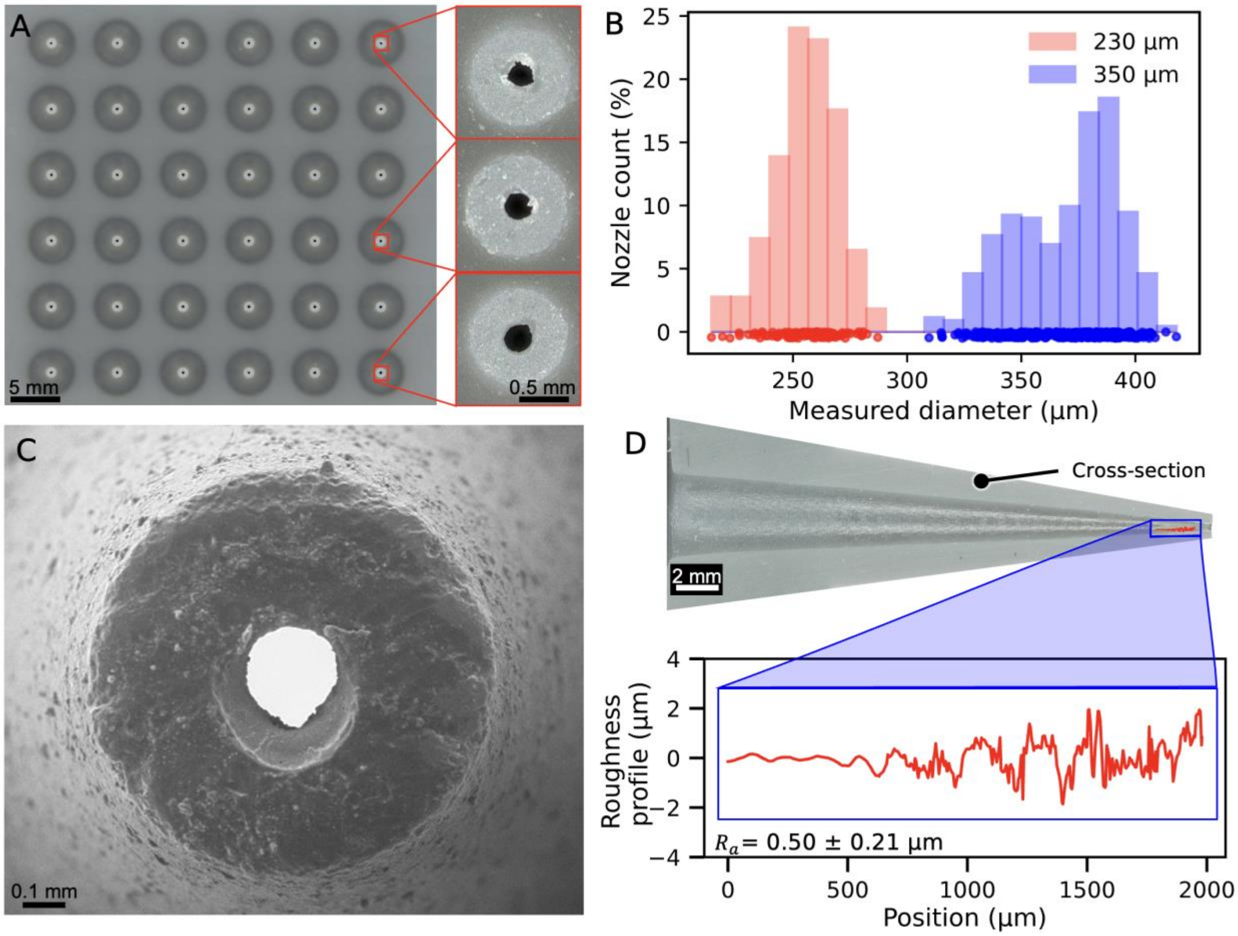

Figure 5.4: (A) Optical microscope image of a representative 6 × 6 multinozzle array with nominal 230 μm outlet diameter, with a magnified view of a single row illustrating outlet size and aperture uniformity. (B) Measured outlet diameter distributions for multinozzle arrays with nominal outlet diameters of 230 μm and 350 μm, based on all 36 outlets per array; the 230 μm geometry was evaluated over 3 arrays (108 outlets total), and the 350 μm geometry over 12 arrays (432 outlets total). (C) SEM image of a representative 230 μm nozzle tip, showing aperture circularity and minor surface texture associated with the layer-wise SLA fabrication process. (D) Cross-sectional view of a longitudinally sectioned tapered channel used for internal surface roughness analysis, with the representative axial measurement region indicated; roughness was measured along the flow direction using multiple line traces and quantified as R_a, reported as mean ± standard deviation.

5.3.6 Position within the DIW Printhead Flow Rate-Outlet Diameter Design Space

To position the selected printhead architecture within the broader DIW design space, the geometric dataset compiled in Table 5.1 was used to compare the predicted performance of multinozzle configurations reported in the literature. Because the published studies employ different materials, rheological conditions, and pressure-delivery systems, directly comparing the experimentally reported flow rates would not provide a consistent basis for design evaluation. Instead, all configurations were re-evaluated using a common analytical framework for cylindrical and tapered channels reported by Brzeski et al. [9], together with the rheological model adopted in the present work. A fixed inlet pressure of 20 MPa, corresponding to the maximum pressure available in the present extrusion system, was imposed for all cases so that differences in predicted printhead flow rate reflect nozzle geometry alone rather than differences in hardware or material system.

For each reported configuration, the flow rate of a single nozzle was first calculated from the reported geometrical parameters, and the total printhead flow rate was then obtained by multiplying by the number of nozzles explicitly demonstrated in the corresponding study. Only experimentally reported nozzle counts were included, so that all plotted configurations represent validated architectures rather than hypothetical extensions.

Figure 5.5 shows the printhead flow rate–outlet diameter map obtained from the normalized comparison. The horizontal axis gives nozzle outlet diameter, and the vertical axis gives total printhead volumetric flow rate. Pictograms identify the corresponding nozzle architecture by indicating the channel geometry (cylindrical or tapered), the multinozzle arrangement (linear or array), and the associated nozzle count. Marker color denotes nozzle length. For architectures available in multiple outlet diameters, continuous curves show how the predicted printhead flow rate varies with outlet diameter while the underlying channel architecture remains unchanged.

Most previously reported DIW architectures operating at sub-millimeter outlet diameters remain confined to relatively low total printhead flow rates under the common pressure condition used here. In particular, the cylindrical configurations cluster in a region below approximately 10^3 $mm^3\ s^{-1}$, reflecting the strong increase in hydraulic resistance as outlet diameter decreases and channel length increases. Higher predicted flow rates are generally associated with either larger outlet diameters or architectures in which throughput is increased primarily through nozzle count rather than by reducing hydraulic resistance.

This map makes explicit the design gap addressed in the present work. Existing multinozzle systems demonstrate the value of parallelization, but most remain limited at fine outlet diameters because they rely on cylindrical channels. The present architecture was developed specifically to overcome this limitation by combining a dense 6×6 grid layout with tapered channels, thereby increasing total printhead flow rate while maintaining sub-millimeter outlet diameters.

In Figure 5.5, the printhead proposed in this work occupies the upper-left region of the map, corresponding to high flow rate at small outlet diameter. For outlet diameters between 250 and 450 µm, the predicted total printhead flow rate of the 36-nozzle tapered architecture reaches values on the order of 10^3–10^4 $mm^3\ s^{-1}$, placing it above the region occupied by previously reported DIW systems evaluated under the same pressure condition.

Although the absolute values depend on the selected rheological model and imposed pressure, the relative structure of the map is governed primarily by nozzle geometry. Within this normalized framework, the comparison shows that the proposed architecture does not simply increase flow rate by adding more nozzles, but shifts the printhead flow rate–outlet diameter trade-off itself. The combination of tapered flow paths and multinozzle parallelization therefore provides a route toward substantially higher DIW build rates while maintaining sub-millimeter outlet diameters.

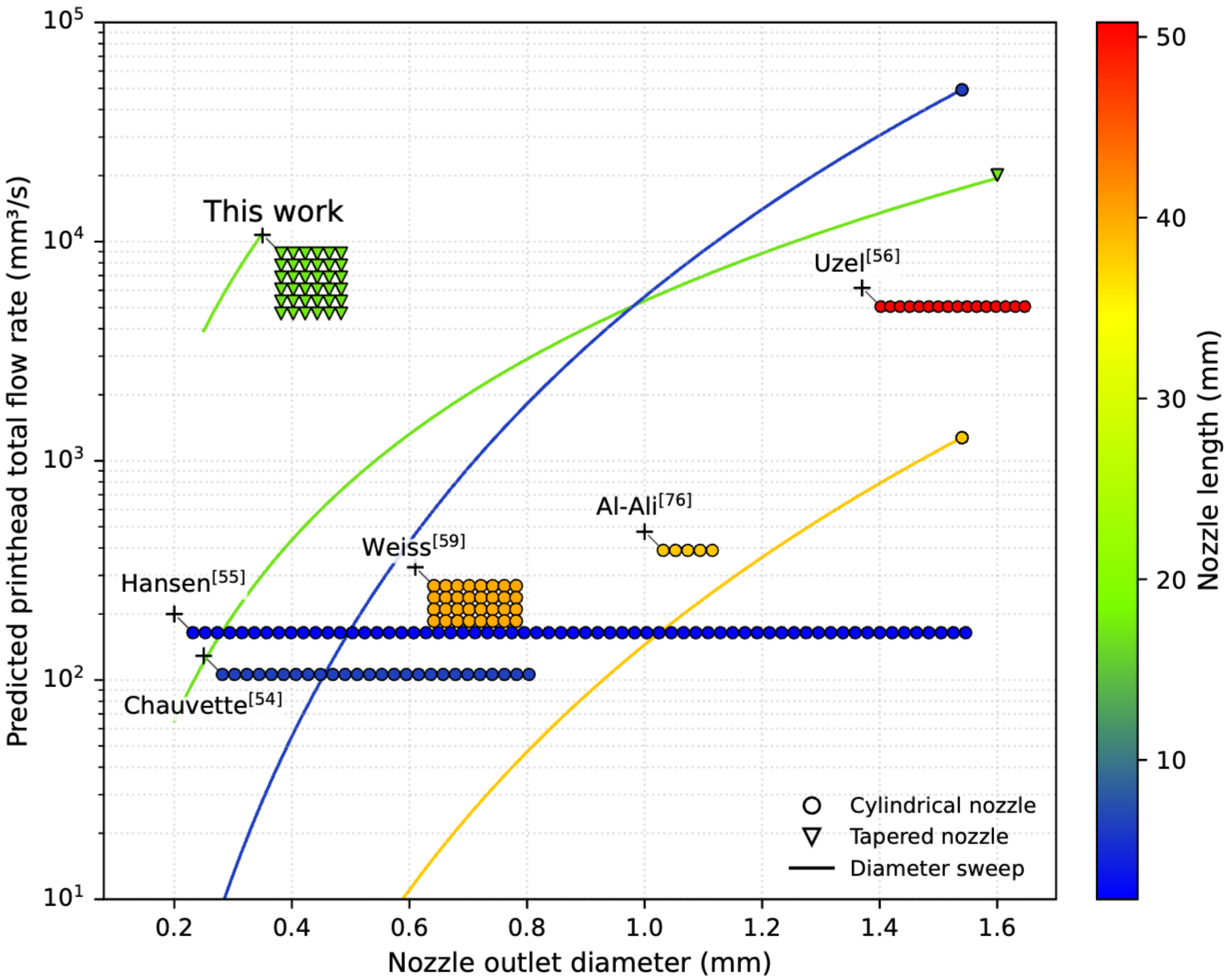

Figure 5.5: Predicted printhead total flow rate as a function of nozzle outlet diameter for different DIW nozzle architectures. For each architecture, the nozzle length is indicated by color using the scale on the right, and the marker pictogram represents nozzle count and layout. Solid lines show the predicted effect of varying nozzle outlet diameter for a fixed channel architecture.

5.4 Printing Demonstration and Fidelity Assessment

5.4.1 Experimental Pressure-Speed response across three material systems

The hydraulic benefit of the tapered multinozzle architecture is evaluated experimentally using three materials spanning a broad range of extrusion difficulty: a wax-based organic reference ink, an EPON 828 thermosetting ink filled with fumed silica, and a highly viscous EC3515 composite modified with 10 wt.% fumed silica. Figure 5.6 shows the measured extrusion pressure as a function of printing speed for each material. In each panel, cylindrical nozzles are represented by circular markers and tapered nozzles by triangular markers. The red dashed horizontal line indicates the 20 MPa pressure limit of the system.

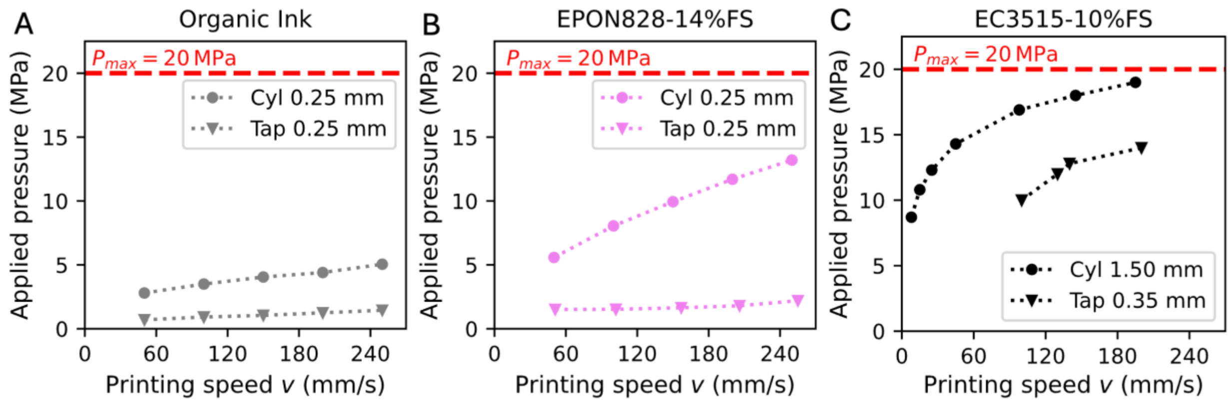

Figure 5.6: Experimental pressure–speed response of cylindrical and tapered multinozzle geometries for three material systems. (A) Organic Ink, (B) EPON 828-14%FS thermosetting ink, (C) EC3515-10%FS composite ink. Circular markers denote cylindrical nozzles and triangular markers denote tapered nozzles. The red dashed horizontal line indicates the maximum available extrusion pressure (20 MPa). Panels (A–B) compare 0.25 mm tapered nozzles with the 0.25 mm cylindrical configuration of Chauvette et al. [13], whereas panel (C) compares a 0.35 mm tapered nozzle with a 1.50 mm cylindrical reference.

For the organic ink (Figure 5.6A) and the EPON 828–14%FS ink (Figure 5.6B), the tapered printhead was evaluated using 250 µm outlet nozzles in order to enable direct comparison with the cylindrical multinozzle architecture reported by Chauvette et al. [54], [61], which also employed 250 µm nozzles with the same materials. It should be noted, however, that the cylindrical reference configuration used a channel length of 6.5 mm, whereas the tapered nozzles used in the present work were 17.25 mm long. Despite this substantially greater length, the tapered geometry consistently operates at lower pressure over the full speed range. At 200 mm s^{-1}, the pressure decreases from 4.4 to 1.25 MPa for the organic ink and from 11.7 to 1.8 MPa for the EPON 828-14%FS ink, corresponding to reductions of 71.6% and 84.6%, respectively. In both cases, extrusion therefore remains well within the system pressure capacity.

A substantially stronger pressure demand was observed for the EC3515-10%FS composite (Figure 5.6C), which is the most viscous material investigated in this work and has not previously been reported in a DIW multinozzle context. In this case, a direct comparison with a 250 µm cylindrical nozzle was not feasible because extrusion at comparable cylindrical diameter would exceed the available system pressure. The successful printing condition used a 350 µm tapered nozzle, and this diameter was therefore retained for the comparison shown in Figure 5.6C. To provide a practical cylindrical benchmark under the same pressure limitation, a much larger 1.50 mm cylindrical nozzle was selected. Even with this substantially larger outlet diameter, the required pressure approaches 20 MPa at 200 mm s^{-1}, whereas the 350 μm tapered nozzle remains below this limit and enabled stable multinozzle extrusion at 200 mm s^{-1} under approximately 15 MPa.

Taken together, the three panels show the same overall trend: extrusion pressure increases with printing speed, but the increase is systematically less pronounced for tapered nozzles than for cylindrical ones. The benefit becomes more consequential as extrusion difficulty increases. For the two lower-resistance materials, tapering provides a substantial quantitative reduction in pressure demand. For the EC3515-10%FS composite, this reduction also has a qualitative consequence, enabling multinozzle extrusion at fine outlet diameter under conditions not accessible to the cylindrical alternative. These results confirm experimentally that tapering enlarges the pressure-speed operating window of multinozzle DIW under a fixed system pressure limit.

5.4.2 Printed Microscaffold Across Material Systems

To examine whether the tapered multinozzle architecture can produce representative periodic scaffolds across materials with distinct rheological behavior, microscaffolds were fabricated using the three formulations introduced in Section 5.4.1. Figure 5.7 presents representative microscaffolds fabricated with the three materials introduced in Section 5.4.1. Figure 5.7A corresponds to the organic reference ink, Figure 5.7B to EPON 828–14%FS, and Figure 5.7C–E to EC3515-10%FS. The associated printing conditions and measured filament dimensions are summarized in Table 5.2.

Table 5.2: Summary of printing conditions and geometric characteristics of microscaffolds fabricated using the tapered multinozzle

Material	**Print speed ($mm \cdot s^{-1}$)**	**Pressure (MPa)**	**Total printhead flow rate ($mm^3\ s^{-1}$)**	**Nominal outlet diameter (μm)**	**Filament width (Mean ± SD, μm)**	**# of layers**
Organic ink	200	1.6	536	350	308 ± 10	20
Epon828-14%FS	50	1.5	134	350	308 ± 35	10
EC3515-10%FS	100	11	545	350	439 ± 27	18

Figure 5.7A shows a scaffold printed with the organic ink at 200 mm s^{-1}. The region visible in the image corresponds to a 36 × 36 filament lattice, obtained from one 36-filament sweep in each

orthogonal direction of successive layers. All 36 filaments remain continuous across the full width of the region shown, indicating uniform extrusion across the array. The enlarged view shows well-defined pores with relatively sharp corners and limited smearing, consistent with controlled deposition. A slight periodic variation in pore size is visible and is attributed to a small mismatch between the printhead orientation and the prescribed deposition angle, which slightly perturbed the intended filament spacing.

Figure 5.7B shows a scaffold printed with the EPON 828–14%FS thermosetting ink at 50 mm s^{-1}. The printed area is smaller than in the organic-ink case, and the magnified region shows interrupted filaments and missing strands, indicating that continuous multinozzle deposition was not fully achieved under these early operating conditions. This behavior is attributed primarily to under-extrusion caused by an imperfect match between extrusion rate and printhead speed. The greater viscoelasticity of this formulation made deposition more sensitive to this mismatch, resulting in reduced geometric regularity relative to the organic-ink scaffold.

The clearest demonstration is provided by the EC3515-10%FS composite, printed at 100 mm s^{-1}. Figure 5.7C shows a representative local region of the scaffold, where filament continuity and pore regularity are both improved relative to the previous cases. Figure 5.7D shows the larger scaffold from which this region was extracted in blue. The structure comprises 108 × 108 filaments in plan view and was fabricated using 3 repeated multinozzle passes per layer with the same 36-nozzle printhead. At this scale, the scaffold retains a high degree of geometric regularity, with limited pore-size variation. Slightly denser filament placement is visible at the extremities of the deposition paths, corresponding to the intended toolpath used to create enclosed edge regions.

Figure 5.7E shows a cross-section of the EC3515-10%FS scaffold through 18 stacked layers. The layer sequence remains clearly distinguishable through the thickness, and bridging between adjacent filaments is maintained without obvious sagging. Some compression is visible in the first few deposited layers near the substrate. This effect is attributed to first-layer height adjustment, which was intentionally tuned to ensure sufficient adhesion to the adhesive tape substrate. Although this leads to local compaction near the base, it does not prevent stable scaffold formation through the remaining build height.

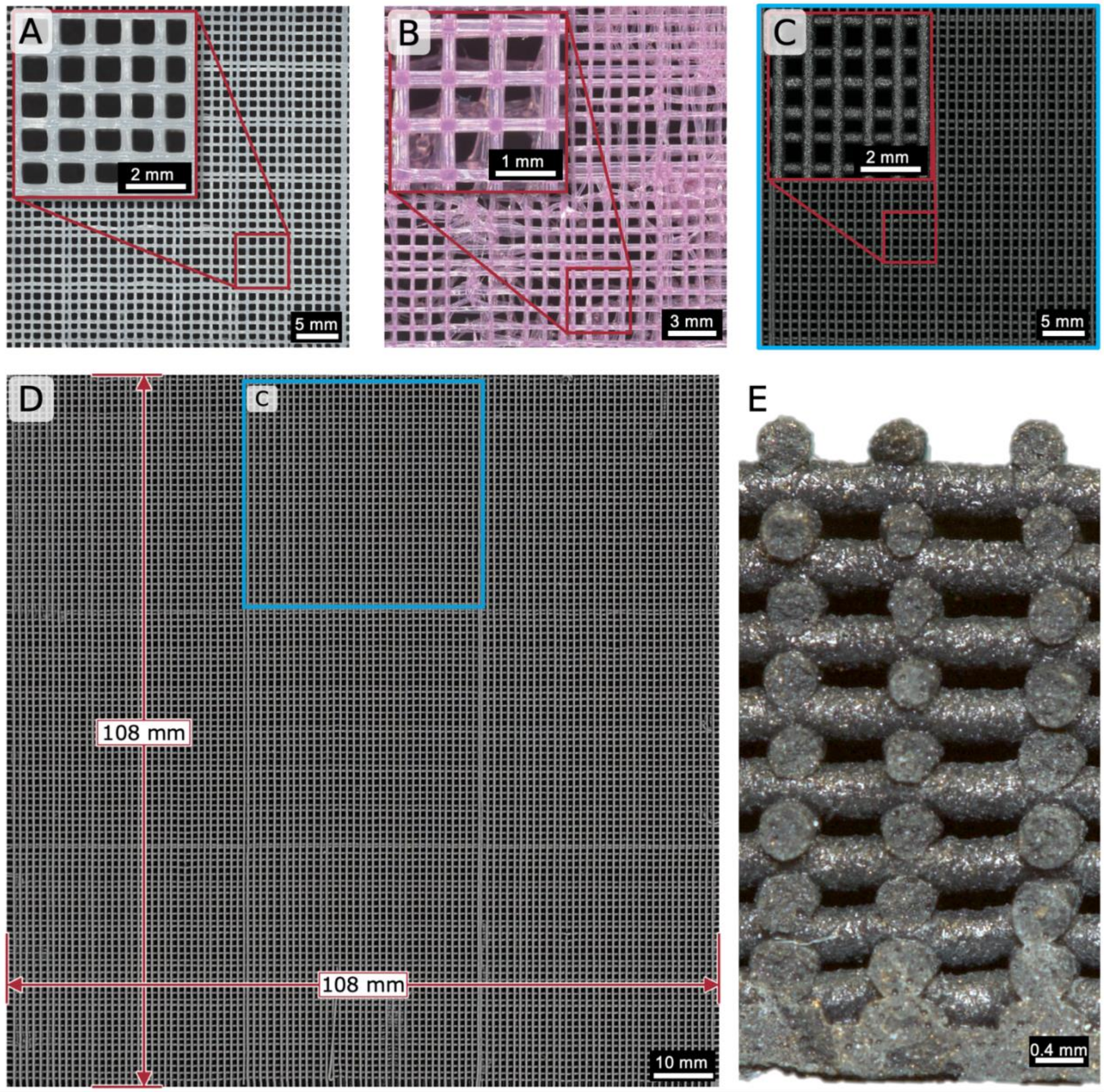

Figure 5.7: Printed microscaffolds obtained with the tapered multinozzle architecture across three material systems. (A) Top view of a 36 × 36 filament scaffold printed with the organic reference ink at 200 mm s^{-1}, with an enlarged region showing the local pore structure. (B) Top view of a scaffold printed with EPON 828–14%FS at 50 mm s^{-1}, showing interrupted filaments and reduced local regularity. (C) Representative local view (blue zone) of a scaffold printed with EC3515-10%FS at 100 mm s^{-1}. (D) Larger view of the EC3515-10%FS scaffold, showing the full printed area and repeated multinozzle deposition pattern. (E) Cross-sectional view of the EC3515-10%FS scaffold, showing the stacked orthogonal filament architecture through 18 layers.

The measured filament widths were 308 ± 10 μm for the organic ink, 308 ± 35 μm for EPON 828–14%FS, and 439 ± 27 μm for EC3515-10%FS. The larger width observed for EC3515-10%FS is consistent with post-extrusion die swell of viscoelastic inks [27], [83]. Overall, Figure 5.7 shows that the selected tapered multinozzle architecture can produce representative periodic microscaffolds across materials of increasing extrusion difficulty, even though the accessible operating conditions differ substantially from one material to another. A representative region extracted from the larger scaffold shown in Figure 5.7D is used in the following section for quantitative geometric fidelity analysis.

5.4.3 Geometric Fidelity of the Printed EC3515-10%FS Microscaffold

To quantify how closely the printed structure reproduced the intended scaffold geometry, a nominal–actual comparison was performed on a representative region extracted from the larger EC3515-10%FS scaffold shown in Figure 5.7D.

Figure 5.8 summarizes the resulting comparison. Figure 5.8A(i) shows the CAD model of the target scaffold, Figure 5.8A(ii) the printed scaffold used for μCT analysis, and Figure 5.8A(iii) the corresponding C2M deviation map. In the deviation map, green is dominant, indicating that most of the printed structure remains close to the nominal geometry. Localized red and blue regions are also present, corresponding respectively to positive and negative deviations relative to the CAD reference. To examine the spatial distribution of these deviations in more detail, Figure 5.8B presents selected slices extracted from the C2M map at different heights through the scaffold. Figure 5.8B(i) shows a top-view slice from the upper portion, represented by B(ii), of the scanned volume. At this height, the pore network remains open and well defined, consistent with the regular top-view morphology already observed in Figure 5.7C–D. Localized positive deviations appear along one side of certain filaments, indicating that some adjacent strands were deposited slightly closer together than prescribed.

A different pattern is observed near the base of the scaffold. Figure 5.8 (iii–iv) shows slices extracted from the lower portion of the structure, where the first deposited layers appear locally compressed into one another and some pores are partially or fully closed over approximately the first 0.5 mm of height. This behavior is consistent with the local compaction already visible in the cross-sectional view of Figure 5.7E and is attributed to first-layer height adjustment used to ensure adhesion to the substrate. Importantly, this deviation pattern is concentrated near the bottom of the structure and does not accumulate progressively through the remaining build height. The overall deviation distribution is summarized in Figure 5.8C, which presents the histogram of C2M signed distances together with the color scale used in the spatial maps. The distribution exhibits a slight positive bias, with a mean signed deviation of +20.0 μm and a median of +19.7 μm, indicating modest overall overbuild relative to the CAD model. The mean absolute deviation was 53.7 µm, while 90% of the surface points fell between −89.7 µm and +126.0 µm. In practical terms, 55.1% of the points remained within ±50 µm of the nominal geometry, and 85.6% remained within ±100 µm. Because the nominal–actual comparison depends on the prior rigid registration step, the reported C2M deviations include a residual alignment component (registration RMS: 74.5 µm), so the small overall positive bias should be interpreted with more caution than the localized spatial deviation patterns.

Finally, Figure 5.8D shows SEM images of the same scaffold sample at increasing magnification. These images provide a qualitative view of the filament surface morphology, which appears rough at the microscale. Angular surface features are visible and are consistent with exposed inclusions or fractured filler particles, although this effect was not quantified in the present work. At the scaffold scale, however, these local surface irregularities do not obscure the underlying lattice architecture demonstrated by the µCT-based comparison.

Together, these results show that the EC3515-10%FS scaffold reproduces the intended lattice geometry with bounded and spatially localized deviations. The most significant departures from the CAD model are concentrated near the substrate, whereas the remainder of the scaffold preserves open pores and a largely regular periodic architecture.

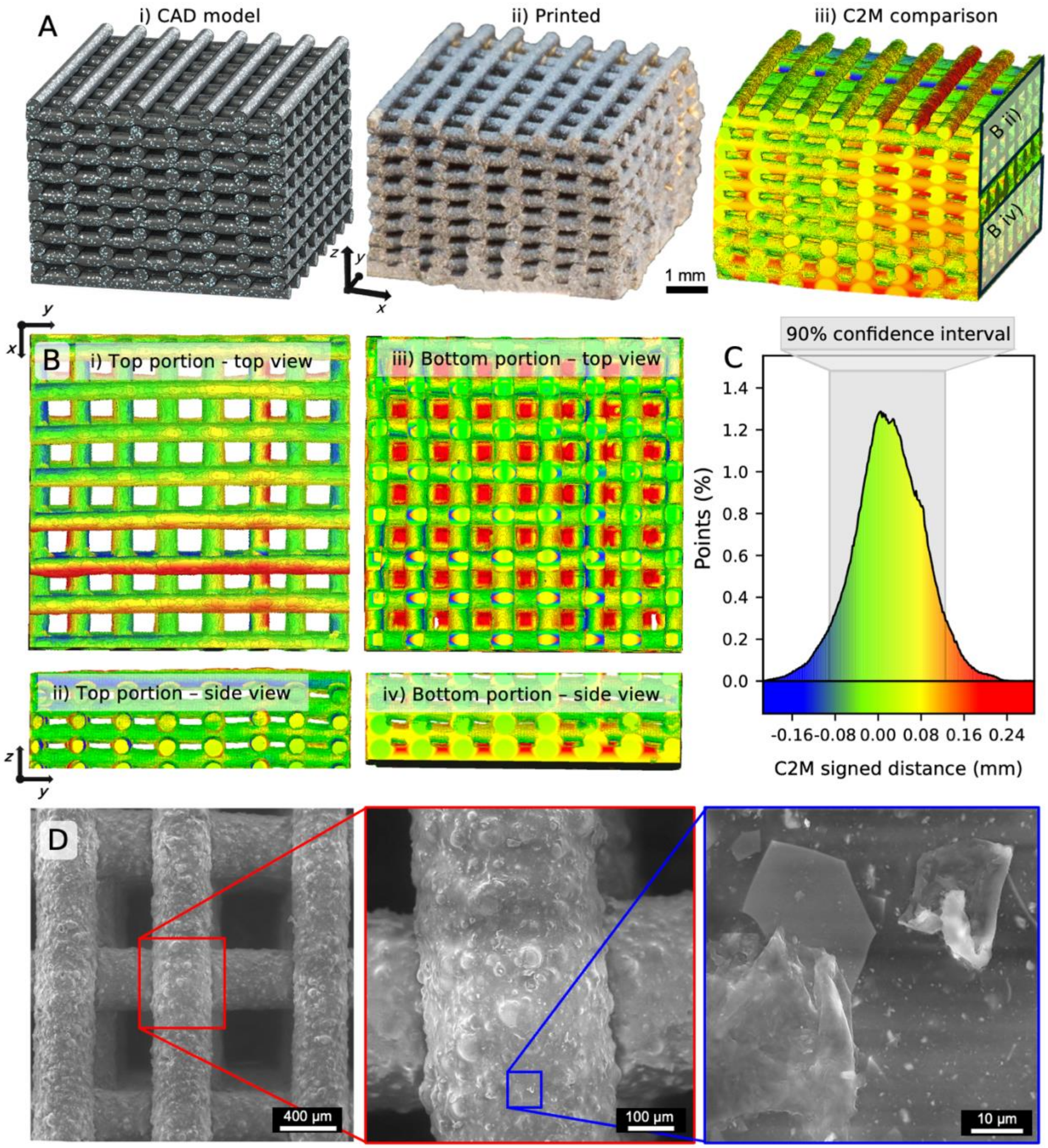

Figure 5.8: Geometric fidelity of the printed EC3515 microscaffold. (A) Comparison between the nominal and printed scaffold geometry: (i) CAD model, (ii) photograph of the printed scaffold used for µCT analysis, and (iii) C2M signed-distance deviation map between the µCT reconstruction and the CAD geometry. (B) Selected slices of the C2M map showing local deviation patterns in the upper and lower portions of the scaffold: (i) top-view slice from the upper region (ii), (iii) top-view slice from the bottom region (iv). (C) Histogram of C2M signed distances, also used as the color scale for the deviation maps, showing a mean signed deviation of +20.0 µm and a 90% central interval of −89.7 to +126.0 µm. (D) SEM images of the same scaffold sample at increasing magnification, showing the surface morphology of the extruded filaments.

5.5 Conclusion

This work demonstrates that combining tapered flow paths with multinozzle parallelization shifts the throughput–resolution trade-off of DIW under practical pressure constraints. The proposed 6 × 6 printhead consists of a semi-disposable SLA-fabricated polymer flow array, intended to be replaceable after use, supported by a reusable machined titanium backing plate that carries the structural load outside the flow path. Finite-element analysis confirmed that tapering substantially reduces hydraulic resistance relative to cylindrical channels of equal outlet diameter, and pressure–speed experiments across three materials of increasing viscosity showed that this advantage translates into a consistently enlarged operating window under the 20 MPa system limit. For the highly viscous EC3515-10%FS composite, stable multinozzle extrusion and scaffold fabrication were achieved at 100 $mm \cdot s^{-1}$ under approximately 11 MPa using 350 μm outlets, whereas comparable cylindrical sub-millimeter configurations were not accessible within the 20 MPa pressure limit. For the representative planar structure considered here, the 36-nozzle configuration reduces the estimated fabrication time from 40.8 h with a single nozzle to 1.1 h at the same deposition speed. Geometric fidelity of the printed EC3515-10%FS scaffold was assessed by μCT-based nominal–actual comparison, yielding a mean signed deviation of +20.0 μm and 85.6% of the surface within ±100 μm of the CAD geometry. The largest deviations were localized near the substrate and did not accumulate through the build height. When positioned against previously reported DIW printhead architectures under a common normalized pressure condition, the proposed design occupies a region of high total flow rate at sub-millimeter outlet diameter not reached by existing cylindrical multinozzle systems. The shift arises from the combination of tapered flow paths and multinozzle parallelization. Beyond throughput, the semi-disposable architecture directly addresses the difficulty of cleaning reactive, particle-filled thermoset composites from reusable multichannel hardware, an operational constraint that becomes increasingly significant as channel diameter decreases and nozzle density increases.

Beyond the specific thermoset scaffold geometries demonstrated here, the combination of semi-disposable flow arrays, tapered channels, and multinozzle parallelization provides a general route for applications where throughput, feature size, and material printability must be balanced simultaneously. In the longer term, this printhead strategy could support larger porous thermoset architectures deposited on complex surfaces, including aerospace clearance-control and acoustic systems where sub-millimeter resolution must be maintained over large areas.

CHAPTER 6 CONCLUSION AND RECOMMENDATIONS

6.1 Summary of Work

This thesis demonstrated that high-throughput direct ink writing of highly viscous thermosetting composites can be achieved under a strict pressure limit of 20 MPa through geometric optimization and architectural redesign of a multinozzle system. Building on the limitations of the previously reported 26-nozzle cylindrical configuration, which was constrained by excessive hydraulic resistance, a tapered multinozzle architecture was designed, fabricated, and experimentally validated. The final implementation consisted of a 6 × 6 (36-nozzle) monolithic SLA-fabricated array reinforced by a machined titanium backing plate. This configuration enabled operation near the 20 MPa system limit while preserving a semi-disposable strategy better suited to reactive thermosetting materials that are difficult to clean from complex multichannel hardware. The selected geometry, comprising a 17.25 mm channel length, a 5.3° half-angle taper, and a nominal 350 µm outlet diameter, was defined to reduce hydraulic resistance without compromising packing density or filament resolution. Experimentally, the tapered architecture consistently reduced the pressure required to reach a given printing speed relative to cylindrical channels. With the industrial glass-microsphere-filled thermosetting composite EC3515 modified with 10 wt.% fumed silica, stable extrusion was achieved at 100 mm/s under 11 MPa. This corresponds to an approximately 200% increase in attainable printing speed relative to a comparable cylindrical configuration under similar pressure constraints. The system enabled total flow rates above 500 mm^3/s while preserving filament diameters in the sub-millimetre range. A representative 18-layer structure comprising 108 parallel filaments per layer was fabricated in under 3.5 minutes, illustrating the build-rate increase enabled by parallelization under pressure-limited conditions. Geometric fidelity was quantitatively verified by µCT-based cloud-to-mesh analysis, which showed a mean deviation of +27 µm and no systematic accumulation of error through layer stacking. In parallel, the digital framework of the platform was adapted to support the new architecture, notably through modifications to the Multinozzle Toolpath Generator and the predictive extrusion model. Overall, this work established that nozzle-scale tapering combined with a semi-disposable multinozzle strategy provides a viable route for pressure-efficient, high-throughput extrusion of highly viscous industrial thermosetting composites.

6.2 Limitations

Despite the demonstrated improvements, several limitations persist.

- **Hydraulic modeling assumption**. The hydraulic comparison was established from nozzle-scale modeling rather than from a full three-dimensional representation of the upstream flow domain. In particular, three-dimensional computational fluid dynamics (CFD) analysis of the reservoir, plenum, and manifold was not performed. Such an approach could be used in future work to predict nozzle-to-nozzle flow partitioning and to assess entry losses associated with the contraction from the manifold into each tapered channel. The present modeling framework also neglected wall slip, particle migration, and extrusion-induced microstructural changes such as hollow-glass-bubble fracture and the associated redistribution of filler.
- **Experimental assessment of flow uniformity**. Although the global pressure-speed response and printed results supported the hydraulic benefit of the retained architecture, individual outlet flow rates were not measured directly. Consequently, flow uniformity across the 36 nozzles was inferred from the printed structures rather than quantified independently. A useful extension would be to compare the measured outlet dimensions of each nozzle before printing with the corresponding dimensions of the extruded filaments, in order to assess nozzle-to-nozzle deposition uniformity more systematically.
- **Material response during extrusion.** Material characterization was focused primarily on extrusion feasibility and printed geometry rather than on microstructural integrity. Particle integrity, filler redistribution, matrix-filler decoupling, and the time-dependent evolution of rheology during extended printing were not quantified systematically. For EC3515-10%FS, the addition of 10 wt.% fumed silica was introduced empirically to obtain enough shape retention, but formulation optimization and post-print abradability were outside the scope of this work.
- **Reuse potential and long-term durability.** The SLA-fabricated multinozzle array was conceived primarily as a replaceable component, which reduces cleaning and maintenance constraints when processing reactive filled thermosetting materials. However, in cases where cleaning can be achieved with acceptable effort, reuse of the same array may become practically relevant. Under such conditions, the long-term behavior of the printed channels remains unknown. In particular, repeated extrusion of particle-filled materials could progressively alter the internal surface or outlet geometry through wear, abrasion, or gradual

material removal, thereby affecting hydraulic resistance and deposition uniformity over time. These effects were not evaluated in the present work.

- **Scalability.** The present work established the feasibility of a 36-nozzle tapered architecture, but the exploration of the design space remained limited. Only a restricted number of geometries were compared experimentally, so the combined influence of channel length, outlet diameter, taper, plenum geometry, and nozzle count was not mapped systematically. Extension beyond the 36-nozzle configuration therefore remains to be demonstrated experimentally.

6.3 Recommendations for Future Work

Future work should focus on the following directions:

- **Material modification during extrusion.** The effect of passage through tapered channels should be assessed more directly, particularly with respect to hollow-glass-bubble integrity, filler redistribution, and the resulting influence on deposited morphology and functional performance.
- **Alternative fabrication routes for the array.** Other vat-photopolymerization approaches, such as projected stereolithography, could be explored to improve dimensional tolerance, repeatability, and geometric fidelity of the fabricated multinozzle arrays.
- **Denser multinozzle architectures.** Higher outlet densities could be investigated to further increase areal deposition rate. This would require revisiting the coupled effects of nozzle length, taper angle, inlet diameter, manufacturable pitch, and resulting filament spacing.
- **Scalable manufacturing of the printhead.** For eventual industrial deployment, replication-based fabrication routes such as molding or casting could be explored to increase production rate and improve reproducibility of the multinozzle component.
- **Non-planar deposition.** Since the targeted applications extend beyond planar substrates, the retained architecture should be evaluated under non-planar robotic printing conditions on representative curved geometries.

6.4 Project Significance

The significance of this work extends beyond the specific demonstrations presented in this thesis. By combining tapered channels, multinozzle parallelization, and a replaceable flow-path component, the proposed architecture establishes a practical strategy for the additive manufacturing of fine thermoset structures under pressure-limited conditions and demonstrates a route toward higher-throughput fabrication. In the immediate context of the project, this strategy supports the development of structured acoustic and abradable coatings for aerospace components. More broadly, it suggests a route toward the additive manufacturing of lightweight reinforced thermoset cores, sandwich-type structures, and other fine structures produced from difficult, highly viscous feedstocks. The project therefore contributes not only a multinozzle printhead, but also a transferable design logic for extending extrusion-based additive manufacturing toward applications where viscosity, feature size, and productivity must be addressed simultaneously.

REFERENCES

[1] R. D. Farahani, L. L. Lebel, and D. Therriault, "Processing parameters investigation for the fabrication of self-supported and freeform polymeric microstructures using ultraviolet-assisted three-dimensional printing," *J. Micromech. Microeng.*, 2014.

[2] Z. Jiang, B. Diggle, M. L. Tan, J. Viktorova, C. W. Bennett, and L. A. Connal, "Extrusion 3D Printing of Polymeric Materials with Advanced Properties," *Advanced Science*, vol. 7, no. 17, p. 2001379, 2020, doi: 10.1002/advs.202001379.

[3] V. G. Rocha, E. Saiz, I. S. Tirichenko, and E. García-Tuñón, "Direct ink writing advances in multi-material structures for a sustainable future," *J. Mater. Chem. A*, vol. 8, no. 31, pp. 15646–15657, 2020, doi: 10.1039/D0TA04181E.

[4] J. Boulvert *et al.*, "Acoustic modeling of micro-lattices obtained by additive manufacturing," *Applied Acoustics*, vol. 164, p. 107244, Jul. 2020, doi: 10.1016/j.apacoust.2020.107244.

[5] J. Costa-Baptista, "Design and fused filament fabrication of multilayered microchannels for subwavelength and broadband sound absorption," *Additive Manufacturing*, 2022.

[6] J.-P. Groby, C. Lagarrigue, B. Brouard, O. Dazel, V. Tournat, and B. Nennig, "Using simple shape three-dimensional rigid inclusions to enhance porous layer absorption," *The Journal of the Acoustical Society of America*, vol. 136, no. 3, pp. 1139–1148, Sep. 2014, doi: 10.1121/1.4892760.

[7] W. Johnston and B. Sharma, "Additive manufacturing of fibrous sound absorbers," *Additive Manufacturing*, vol. 41, p. 101984, May 2021, doi: 10.1016/j.addma.2021.101984.

[8] J. Huang *et al.*, "A comprehensive review of thermally sprayed abradable sealing coatings: Focusing on abradability," *Chinese Journal of Aeronautics*, vol. 37, no. 10, pp. 1–25, Oct. 2024, doi: 10.1016/j.cja.2024.08.014.

[9] D. Brzeski, "Development of Thermosetting Composite Materials for Producing Multifunctional Coatings by Direct Ink Writing," masters, Polytechnique Montréal, 2021. Accessed: Mar. 08, 2026. [Online]. Available: https://publications.polymtl.ca/9131/

[10] J.-F. Chauvette, "Non-Planar Multinozzle Additive Manufacturing of Thermoset Composites," phd, Polytechnique Montréal, 2023. Accessed: Feb. 16, 2026. [Online]. Available: https://publications.polymtl.ca/53426/

[11] K. T. Estelle and B. A. Gozen, "Complex ink flow mechanisms in micro-direct-ink-writing and their implications on flow rate control," *Additive Manufacturing*, vol. 59, p. 103183, Nov. 2022, doi: 10.1016/j.addma.2022.103183.

[12] A. Marnot, K. Koube, S. Jang, N. Thadhani, J. Kacher, and B. Brettmann, "Material extrusion additive manufacturing of high particle loaded suspensions: a review of materials, processes and challenges," *Virtual and Physical Prototyping*, vol. 18, no. 1, p. e2279149, Dec. 2023, doi: 10.1080/17452759.2023.2279149.

[13] I. Gibson, D. Rosen, B. Stucker, and M. Khorasani, *Additive Manufacturing Technologies*. Cham: Springer International Publishing, 2021. doi: 10.1007/978-3-030-56127-7.

[14] J. A. Lewis, "Direct Ink Writing of 3D Functional Materials," *Adv Funct Materials*, vol. 16, no. 17, pp. 2193–2204, Nov. 2006, doi: 10.1002/adfm.200600434.

[15] M. A. S. R. Saadi *et al.*, “Direct Ink Writing: A 3D Printing Technology for Diverse Materials,” *Advanced Materials*, vol. 34, no. 28, p. 2108855, Jul. 2022, doi: 10.1002/adma.202108855.

[16] J. C. III and P. D. Calvert, “Freeforming objects with low-binder slurry,” US6027326A, Feb. 22, 2000 Accessed: Jan. 05, 2026. [Online]. Available: https://patents.google.com/patent/US6027326A/en

[17] J. A. Lewis and G. M. Gratson, “Direct writing in three dimensions,” *Materials Today*, vol. 7, no. 7–8, pp. 32–39, Jul. 2004, doi: 10.1016/s1369-7021(04)00344-x.

[18] J. E. Smay, J. Cesarano, and J. A. Lewis, “Colloidal Inks for Directed Assembly of 3-D Periodic Structures,” *Langmuir*, vol. 18, no. 14, pp. 5429–5437, Jul. 2002, doi: 10.1021/la0257135.

[19] R. L. Truby and J. A. Lewis, “Printing soft matter in three dimensions,” *Nature*, vol. 540, no. 7633, pp. 371–378, Dec. 2016, doi: 10.1038/nature21003.

[20] V. I. Dos Santos, J. Chevalier, M. C. Fredel, B. Henriques, and L. Gremillard, “Ceramics and ceramic composites for biomedical engineering applications via Direct Ink Writing: Overall scenario, advances in the improvement of mechanical and biological properties and innovations,” *Materials Science and Engineering: R: Reports*, vol. 161, p. 100841, Dec. 2024, doi: 10.1016/j.mser.2024.100841.

[21] B. G. Compton and J. A. Lewis, “3D-Printing of Lightweight Cellular Composites,” *Advanced Materials*, vol. 26, no. 34, pp. 5930–5935, Sep. 2014, doi: 10.1002/adma.201401804.

[22] D. A. Rau, M. J. Bortner, and C. B. Williams, “A rheology roadmap for evaluating the printability of material extrusion inks,” *Additive Manufacturing*, vol. 75, p. 103745, Aug. 2023, doi: 10.1016/j.addma.2023.103745.

[23] R. G. Larson and Y. Wei, “A review of thixotropy and its rheological modeling,” *J. Rheol.*, vol. 63, no. 3, pp. 477–501, May 2019, doi: 10.1122/1.5055031.

[24] Z. Guo, F. Fei, X. Song, and C. Zhou, “Analytical Study and Experimental Verification of Shear-Thinning Ink Flow in Direct Ink Writing Process,” *Journal of Manufacturing Science and Engineering*, vol. 145, no. 7, p. 071001, Jul. 2023, doi: 10.1115/1.4056926.

[25] H. Herrada-Manchón, M. A. Fernández, and E. Aguilar, “Essential Guide to Hydrogel Rheology in Extrusion 3D Printing: How to Measure It and Why It Matters?,” *Gels*, vol. 9, no. 7, p. 517, Jun. 2023, doi: 10.3390/gels9070517.

[26] A. Nicolas, E. E. Ferrero, K. Martens, and J.-L. Barrat, “Deformation and flow of amorphous solids: Insights from elastoplastic models,” *Rev. Mod. Phys.*, vol. 90, no. 4, p. 045006, Dec. 2018, doi: 10.1103/RevModPhys.90.045006.

[27] L. M. Friedrich and J. E. Seppala, “Simulated filament shapes in embedded 3D printing,” *Soft Matter*, vol. 17, no. 35, pp. 8027–8046, Sep. 2021, doi: 10.1039/D1SM00731A.

[28] M. Hayek, Y. E. Bitouri, K. Bouarab, and A. Yahia, “Structural Build-Up of Cement Pastes: A Comprehensive Overview and Key Research Directions,” *Construction Materials*, vol. 5, no. 2, May 2025, doi: 10.3390/constrmater5020031.

[29] J. Mewis and N. J. Wagner, *Colloidal suspension rheology*. in Cambridge series in chemical engineering. Cambridge ; New York: Cambridge University Press, 2012.

[30] R. B. Bird, R. C. Armstrong, and O. Hassager, *Dynamics of polymeric liquids*, 2nd éd. New York Chichester Brisbane [etc.]: J. Wiley and sons, 1987.

[31] M. Bek, J. Gonzalez-Gutierrez, C. Kukla, K. Pušnik Črešnar, B. Maroh, and L. Slemenik Perše, "Rheological Behaviour of Highly Filled Materials for Injection Moulding and Additive Manufacturing: Effect of Particle Material and Loading," *Applied Sciences*, vol. 10, no. 22, p. 7993, Nov. 2020, doi: 10.3390/app10227993.

[32] P. Wilms, J. Wieringa, T. Blijdenstein, K. van Malssen, and R. Kohlus, "Quantification of shear viscosity and wall slip velocity of highly concentrated suspensions with non-Newtonian matrices in pressure driven flows," *Rheol Acta*, vol. 60, no. 8, pp. 423–437, Aug. 2021, doi: 10.1007/s00397-021-01281-5.

[33] E. Luzzi, M. De Salzano De Luna, D. Caputo, G. Filippone, and P. Aprea, "Printability Metrics in Direct Ink Writing: Critical Review of the Literature and Novel Perspective Based on Dimensional Analysis," *Adv Materials Technologies*, vol. 10, no. 22, p. e01282, Nov. 2025, doi: 10.1002/admt.202501282.

[34] C. W. Macosko, Ed., *Rheology: principles, measurements, and applications*. in Advances in interfacial engineering series. New York: VCH, 1994.

[35] E. M. Petrie, *Epoxy adhesive formulations*. New York: McGraw-Hill, 2006.

[36] V. Ambrogi, S. Cosco, C. Carfagna, G. Cicala, L. Oliveri, and A. Recca, "Comparison of the effect of epoxy microspheres on the thermomechanical and rheological properties of an epoxy resin system," *Polymer Engineering & Sci*, vol. 46, no. 12, pp. 1739–1747, Dec. 2006, doi: 10.1002/pen.20647.

[37] S. K. Romberg and A. P. Kotula, "Simultaneous rheology and cure kinetics dictate thermal post-curing of thermoset composite resins for material extrusion," *Additive Manufacturing*, vol. 71, p. 103589, Jun. 2023, doi: 10.1016/j.addma.2023.103589.

[38] I. E. Idelchik, *Handbook of Hydraulic Resistance, 4th Edition Revised and Augmented*. Begell House Inc., 2008. doi: 10.1615/978-1-56700-251-5.0.

[39] D. C. Rennels and H. M. Hudson, *Pipe Flow: A Practical and Comprehensive Guide*, 1st ed. Wiley, 2012. doi: 10.1002/9781118275276.

[40] J. Bruneaux, D. Therriault, and M.-C. Heuzey, "Micro-extrusion of organic inks for direct-write assembly," *J. Micromech. Microeng.*, vol. 18, no. 11, p. 115020, Nov. 2008, doi: 10.1088/0960-1317/18/11/115020.

[41] A. Pricci, M. D. D. Tullio, and G. Percoco, "Semi-analytical models for non-Newtonian fluids in tapered and cylindrical ducts, applied to the extrusion-based additive manufacturing," *Materials & Design*, vol. 223, p. 111168, Nov. 2022, doi: 10.1016/j.matdes.2022.111168.

[42] T. V. How and R. A. Black, "Pressure losses in non-Newtonian flow through rigid wall tapered tubes," *BIR*, vol. 24, no. 3, pp. 337–351, Jun. 1987, doi: 10.3233/bir-1987-24306.

[43] T. Jiang, Z. Huang, J. Li, Y. Zhou, and C. Xiong, "Effect of Nozzle Geometry on the Flow Dynamics and Resistance Inside and Outside the Cone-Straight Nozzle," *ACS Omega*, vol. 7, no. 11, pp. 9652–9665, Mar. 2022, doi: 10.1021/acsomega.1c07050.

[44] A. Royne and C. J. Dey, "Effect of nozzle geometry on pressure drop and heat transfer in submerged jet arrays," *International Journal of Heat and Mass Transfer*, vol. 49, no. 3–4, pp. 800–804, Feb. 2006, doi: 10.1016/j.ijheatmasstransfer.2005.11.014.

[45] S. Marion, "Improved printability and electrical conductivity of carbon black polymer composite with a customized nozzle of material extrusion process," *Additive Manufacturing*, 2024.

[46] T. Schuller, "Optimal shape design of printing nozzles for extrusion-based additive manufacturing," *Additive Manufacturing*, 2024.

[47] A. W. Chen and E. M. Sparrow, "Systematic Approaches for Design of Distribution Manifolds Having the Same Per-Port Outflow," *Journal of Fluids Engineering*, vol. 131, no. 6, p. 061101, Jun. 2009, doi: 10.1115/1.3111256.

[48] H. Liu and P. Li, "Even distribution/dividing of single-phase fluids by symmetric bifurcation of flow channels," *International Journal of Heat and Fluid Flow*, vol. 40, pp. 165–179, Apr. 2013, doi: 10.1016/j.ijheatfluidflow.2013.01.011.

[49] J. Wang, "Theory of flow distribution in manifolds," *Chemical Engineering Journal*, vol. 168, no. 3, pp. 1331–1345, Apr. 2011, doi: 10.1016/j.cej.2011.02.050.

[50] J. Wang and H. Wang, "Discrete method for design of flow distribution in manifolds," *Applied Thermal Engineering*, vol. 89, pp. 927–945, Oct. 2015, doi: 10.1016/j.applthermaleng.2015.06.069.

[51] M. Biedermann and M. Meboldt, "Computational design synthesis of additive manufactured multi-flow nozzles," *Additive Manufacturing*, vol. 35, p. 101231, Oct. 2020, doi: 10.1016/j.addma.2020.101231.

[52] O. S. Carneiro, J. M. Nóbrega, P. J. Oliveira, and F. T. Pinho, "Flow Balancing in Extrusion Dies for Thermoplastic Profiles," 2003.

[53] N. Hagioka, H. Fukuoka, Y. Minegishi, and K. Kodama, "Application of Computational Fluid Dynamics to Design of Polymer Extrusion Dies," *IOP Conf. Ser.: Mater. Sci. Eng.*, vol. 501, p. 012061, Apr. 2019, doi: 10.1088/1757-899X/501/1/012061.

[54] J.-F. Chauvette, D. Brzeski, I. L. Hia, R. D. Farahani, N. Piccirelli, and D. Therriault, "High-speed multinozzle additive manufacturing and extrusion modeling of large-scale microscaffold networks," *Additive Manufacturing*, vol. 47, p. 102294, Nov. 2021, doi: 10.1016/j.addma.2021.102294.

[55] D. C. J. Hansen, D. B. Kolesky, J. J. Vericella, S. J. Kranz, and J. A. Lewis, "High-Throughput Printing via Microvascular Multinozzle Arrays," *Adv. Mater.*, 2013.

[56] S. G. M. Uzel, R. D. Weeks, M. Eriksson, D. Kokkinis, and J. A. Lewis, "Multimaterial Multinozzle Adaptive 3D Printing of Soft Materials," *Adv Materials Technologies*, vol. 7, no. 8, p. 2101710, Aug. 2022, doi: 10.1002/admt.202101710.

[57] M. Al-Ali and Y. Almubarak, "Compact multi-nozzle 3D printer for multi-material direct ink writing using bent needles," *Int J Adv Manuf Technol*, vol. 141, no. 7, pp. 3815–3827, Dec. 2025, doi: 10.1007/s00170-025-16874-0.

[58] M. A. Skylar-Scott, J. Mueller, C. W. Visser, and J. A. Lewis, “Voxelated soft matter via multimaterial multinozzle 3D printing,” *Nature*, vol. 575, no. 7782, pp. 330–335, Nov. 2019, doi: 10.1038/s41586-019-1736-8.

[59] J. D. Weiss *et al.*, “A Low-Cost, Open-Source 3D Printer for Multimaterial and High-Throughput Direct Ink Writing of Soft and Living Materials,” *Advanced Materials*, vol. 37, no. 10, p. 2414971, Mar. 2025, doi: 10.1002/adma.202414971.

[60] J. Chauvette *et al.*, “Non-Planar Multiprocess Additive Manufacturing of Multifunctional Composites,” *Adv Materials Technologies*, vol. 8, no. 17, p. 2300399, Sep. 2023, doi: 10.1002/admt.202300399.

[61] J.-F. Chauvette, I. L. Hia, R. D. Farahani, R. Plante, N. Piccirelli, and D. Therriault, “Non-planar multinozzle additive manufacturing of thermoset composite microscaffold networks,” *Composites Part B: Engineering*, vol. 256, p. 110627, May 2023, doi: 10.1016/j.compositesb.2023.110627.

[62] J. Giboz, T. Copponnex, and P. Mélé, “Microinjection molding of thermoplastic polymers: a review,” *J. Micromech. Microeng.*, vol. 17, no. 6, pp. R96–R109, Jun. 2007, doi: 10.1088/0960-1317/17/6/R02.

[63] K. H. Ho and S. T. Newman, “State of the art electrical discharge machining (EDM),” *International Journal of Machine Tools and Manufacture*, vol. 43, no. 13, pp. 1287–1300, Oct. 2003, doi: 10.1016/S0890-6955(03)00162-7.

[64] S. Scott and Z. Ali, “Fabrication Methods for Microfluidic Devices: An Overview,” *Micromachines*, vol. 12, no. 3, p. 319, Mar. 2021, doi: 10.3390/mi12030319.

[65] P. Singh, A. Pramanik, A. K. Basak, C. Prakash, and V. Mishra, “Developments of non-conventional drilling methods—a review,” *Int J Adv Manuf Technol*, vol. 106, no. 5–6, pp. 2133–2166, Jan. 2020, doi: 10.1007/s00170-019-04749-0.

[66] Q. Ge *et al.*, “Projection micro stereolithography based 3D printing and its applications,” 2020.

[67] C. F. Ceballos-González *et al.*, “Plug-and-Play Multimaterial Chaotic Printing/Bioprinting to Produce Radial and Axial Micropatterns in Hydrogel Filaments,” *Advanced Materials Technologies*, vol. 8, no. 17, p. 2202208, 2023, doi: 10.1002/admt.202202208.

[68] S. C. Millik *et al.*, “3D printed coaxial nozzles for the extrusion of hydrogel tubes toward modeling vascular endothelium,” *Biofabrication*, vol. 11, no. 4, p. 045009, Jul. 2019, doi: 10.1088/1758-5090/ab2b4d.

[69] J. Mueller, J. R. Raney, K. Shea, and J. A. Lewis, “Architected Lattices with High Stiffness and Toughness via Multicore–Shell 3D Printing,” *Advanced Materials*, vol. 30, no. 12, p. 1705001, 2018, doi: 10.1002/adma.201705001.

[70] N. M. Larson, J. Mueller, A. Chortos, Z. S. Davidson, D. R. Clarke, and J. A. Lewis, “Rotational multimaterial printing of filaments with subvoxel control,” *Nature*, vol. 613, no. 7945, pp. 682–688, Jan. 2023, doi: 10.1038/s41586-022-05490-7.

[71] H. M. Wyss, D. L. Blair, J. F. Morris, H. A. Stone, and D. A. Weitz, “Mechanism for clogging of microchannels,” *Phys. Rev. E*, vol. 74, no. 6, p. 061402, Dec. 2006, doi: 10.1103/PhysRevE.74.061402.

[72] J.-F. Chauvette, I. L. Hia, R. D. Farahani, R. Plante, N. Piccirelli, and D. Therriault, "Non-planar multinozzle additive manufacturing of thermoset composite microscaffold networks," *Composites Part B: Engineering*, vol. 256, p. 110627, May 2023, doi: 10.1016/j.compositesb.2023.110627.

[73] R. Ajdary *et al.*, "Direct Ink Writing of Biocompatible Nanocellulose and Chitosan Hydrogels for Implant Mesh Matrices," 2022.

[74] J. Pierre, F. Iervolino, R. D. Farahani, N. Piccirelli, M. Lévesque, and D. Therriault, "Material extrusion additive manufacturing of multifunctional sandwich panels with load-bearing and acoustic capabilities for aerospace applications," *Additive Manufacturing*, vol. 61, p. 103344, Jan. 2023, doi: 10.1016/j.addma.2022.103344.

[75] J. Pierre *et al.*, "Non-planar material-extrusion additive manufacturing of multifunctional sandwich structures using carbon-reinforced polyetheretherketone (PEEK)," *Additive Manufacturing*, vol. 84, p. 104124, Mar. 2024, doi: 10.1016/j.addma.2024.104124.

[76] M. Al-Ali and Y. Almubarak, "Compact multi-nozzle 3D printer for multi-material direct ink writing using bent needles," *The International Journal of Advanced Manufacturing Technology*.

[77] M. Li, X. Tian, D. J. Schreyer, and X. Chen, "Effect of needle geometry on flow rate and cell damage in the dispensing-based biofabrication process," *Biotechnology Progress*, vol. 27, no. 6, pp. 1777–1784, Nov. 2011, doi: 10.1002/btpr.679.

[78] D. L. B. Paul and P. A. Susila, "Direct ink writing of bioceramic prosthetics and scaffolds: advances, challenges, and biomedical applications," *Prog Addit Manuf*, vol. 10, no. 9, pp. 5829–5850, Sep. 2025, doi: 10.1007/s40964-025-01002-x.

[79] D. Therriault, S. R. White, and J. A. Lewis, "Rheological Behavior of Fugitive Organic Inks for Direct-Write Assembly," *Applied Rheology*, vol. 17, no. 1, pp. 10112-1-10112–8, Feb. 2007, doi: 10.1515/arh-2007-0001.

[80] "General Purpose Dispense Tips." Accessed: Dec. 11, 2025. [Online]. Available: https://www.nordson.com/en/products/efd-products/general-purpose-dispense-tips

[81] F. M. White, *Viscous Fluid Flow*. McGraw-Hill Education, 2005.

[82] E. Mitsoulis and S. G. Hatzikiriakos, "Bagley correction: the effect of contraction angle and its prediction," *Rheologica Acta*, vol. 42, no. 4, pp. 309–320, Jul. 2003, doi: 10.1007/s00397-003-0294-y.

[83] P. Wei, C. Cipriani, C.-M. Hsieh, K. Kamani, S. Rogers, and E. Pentzer, "Go with the flow: Rheological requirements for direct ink write printability," *Journal of Applied Physics*, vol. 134, no. 10, p. 100701, Sep. 2023, doi: 10.1063/5.0155896.

[84] D. Brzeski *et al.*, "Design of thermoset composites for high-speed additive manufacturing of lightweight sound absorbing micro-scaffolds," *Additive Manufacturing*, vol. 47, p. 102245, Nov. 2021, doi: 10.1016/j.addma.2021.102245.

APPENDIX A EXTENSION OF THE MEPM TO TAPERED GEOMETRIES

The Multinozzle Extrusion Prediction Model (MEPM), originally developed for cylindrical multinozzle geometries [54], was extended in this project to account for tapered channels. The model provides a rapid predictive tool for comparing cylindrical and tapered configurations under a common pressure limit.

In its original form, MEPM estimates admissible printing conditions as a function of printhead geometry, material rheology, and pressure limit. For cylindrical geometries, the nozzle pressure drop is written as

$$\Delta P = Q_i R_i \qquad \text{(A.1)}$$

where Q_i is the volumetric flow contribution associated with the considered geometry and R_i the corresponding hydraulic resistance term. This product form was retained to preserve compatibility with the existing code structure.

To account for tapered geometries, an analytical expression for power-law flow in conical channels was introduced [84]. The volumetric flow rate Q_T for a tapered nozzle of exit diameter D_{out}, entry diameter D_{in}, and half-angle θ is written as

$$Q_T = \frac{\pi D_{out}^3 D_{in}^3}{32}\left[\frac{3n_a \Delta P \tan\,\theta}{2K_a\left(D_{in}^{3n_a} - D_{out}^{3n_a}\right)}\right]^{1/n_a} \qquad \text{(A.2)}$$

where K_a and n_a are the apparent power-law consistency and flow indices, respectively.

To incorporate this relation without restructuring the original cylindrical framework, Eq. (A.2) was rearranged into a form consistent with Eq. (A.1). Solving for pressure gives

$$\Delta P = Q_T^{n_a}\left(\frac{32}{\pi D_{out}^3 D_{in}^3}\right)^{n_a} \frac{2K_a\left(D_{in}^{3n_a} - D_{out}^{3n_a}\right)}{3n_a \tan\,\theta} \qquad \text{(A.3)}$$

which may be written formally as

$$Q_i \equiv Q_T^{n_a} \qquad \text{(A.4)}$$

$$R_i \equiv \left(\frac{32}{\pi D_i^3 D_e^3}\right)^{n_a} \frac{2K_a\left(D_e^{3n_a} - D_i^{3n_a}\right)}{3n_a \tan\ \theta} \qquad \text{(A.5)}$$

In this context, Q_i and R_i are algebraic placeholders introduced for coding consistency rather than direct physical analogues of the cylindrical formulation.

APPENDIX B EXTENSION OF THE MTG

B1. Limitation of the Original MTG

The original MTG was developed to generate planar and non-planar microscaffold toolpaths using an odd number of passes per layer in each principal direction. This constraint simplifies sequencing because the first and last pass of a layer share the same travel direction. After two layers, the tool therefore returns to a consistent starting pose, allowing the planner to close a two-layer cycle. The corresponding logic is summarized in Table B.1, and the resulting periodic behavior is illustrated in Figure B.1.

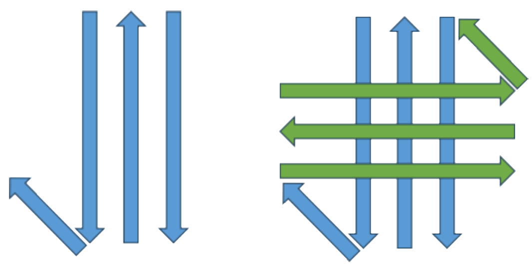

Figure B.1: Schematic representation of the 2-layer cycle required to restore path periodicity under odd pass conditions

However, this formulation breaks down when an even number of passes per layer is introduced. In that case, the first and last pass directions become opposite, and the tool no longer returns to the same starting pose after two layers. The original two-layer cyclic assumption is therefore no longer valid.

Table B.1: Sequencing logic of the original MTG formulation for odd pass counts

<table>
<tr><th>Layer</th><th>First | Last Pass Direction</th><th>Connection Direction (in between)</th><th>Connection Direction (to next pass)</th><th>First | Last bleed</th><th>Change Orientation</th></tr>
<tr><td>0</td><td>+Y | +Y</td><td>(same Y direction), -X</td><td>(Next pass Y dir), -X</td><td>+Y | +Y</td><td>-X, -Y</td></tr>
<tr><td>1</td><td>+X | +X</td><td>(same X dir), -Y</td><td>(Next X dir), -Y</td><td>+X | +X</td><td>-X, -Y</td></tr>
</table>

B2. Four-Layer State Machine for Even Pass Counts

To accommodate even pass counts while preserving deterministic cyclic behavior, the MTG logic was extended to a four-layer state machine. Instead of closing the sequence every two layers, the modified planner closes it every four layers. Within this formulation, pass direction, connection direction, and bleed logic evolve deterministically over four successive layers. After the fourth layer, the tool returns to the initial starting pose of layer 0, thereby restoring periodicity. The corresponding logic is illustrated in Figure B.2 and summarized in Table B.2.

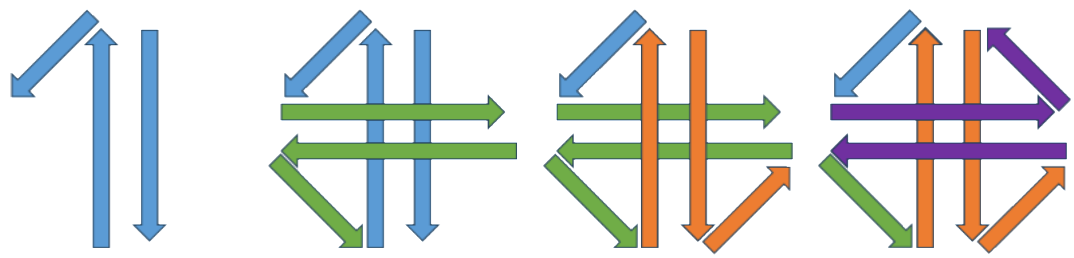

Figure B.2: Schematic representation of the four-layer cycle required to restore path periodicity under even pass conditions

Table B.2: Sequencing logic of the generalized four-layer MTG formulation for even pass counts

Layer	First | Last Pass Direction	Connection Direction (in between)	Connection Direction (to next pass)	First | Last bleed	Change Orientation
0	+Y | -Y	(same Y dir), -X	(Next pass Y dir), -X	+Y | -Y	-X, +Y
1	+X | -X	(same X dir), +Y	(Next X dir), +Y	+X | -X	+X, +Y
2	-Y | +Y	(same Y dir),+X	(Next Y dir),+X	-Y | +Y	+X, -Y
3	-X | +X	(same X dir), -Y	(Next X dir), -Y	-X | +X	-X, -Y